

# Electronic Spectroscopy of Topological Superconductor $\text{FeTe}_{(1-x)}\text{Se}_x$

Mason J. Gray

A dissertation  
submitted to the Faculty of  
the department of Physics  
in partial fulfillment  
of the requirements  
for the degree of  
Doctor of Philosophy

Boston College  
Morrissey College of Arts and Sciences  
Graduate School

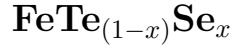
May 2021



# Todo list

Finish acknowledgements page . . . . .	v
Write introduction on topology and fabrication. . . . .	1
After writing proper intro, come back and make this flow. . . . .	2
After edits to Chapter 2, come back and make this flow. . . . .	14
Write exciting new results in FTS along with questions left to verify. . . . .	27
cite Andrea's work on different transport characteristics of graphene . . . . .	27
cite klein paper . . . . .	28
Make Edge vs Plateau figure . . . . .	28
fig ref . . . . .	28
cite field work . . . . .	30
Write summary of FTS and glovebox. Give ideas for new experiments. . . . .	33

# Electronic Spectroscopy of Topological Superconductor



Mason J. Gray

Advisor: Kenneth S. Burch, Ph.D.

## ABSTRACT

In condensed matter physics we study the behavior of crystals at finite density and low temperatures. By tuning and breaking the various materials, symmetries, and the topology of a crystal one can bring about brand new quantum phases of matter. These new phases of matter in turn produce emergent quasiparticles such as the cooper pair in superconductivity, the spinon in magnetic systems, and the Fermi arcs in Weyl semimetals.

Of particular interest are systems in which superconductivity interacts with topology. These systems have been theoretically predicted to produce anyonic quasiparticles which may be used as qubits in a future fault-tolerant quantum computer. However, these system usually require the use of the superconducting proximity effect to inject cooper pairs into the topological system. This is turn requires interfacing two different materials which not only requires extremely clean interfaces, but also matching Fermi surfaces, comparable Fermi velocities, and more. The ideal candidate for topological superconductivity would therefore be a material that is both superconducting and topologically non-trivial. One promising candidate is the iron-based superconductor  $\text{FeTe}_{(1-x)}\text{Se}_x$ , specifically the at  $\text{FeTe}_{0.45}\text{Se}_{0.55}$  (FTS) doping which also has non-trivial topology. In this dissertation we address the fabrication of pristine interfaces using a new tool as well as new probes into the topology of FTS.

In Chapter II we discuss the motivation, construction, and use of the “cleanroom-in-a-glovebox”. This tool places an entire nanofabrication workflow into an inert argon atmosphere which has allowed us access to study a myriad of new materials and systems. A delightful offshoot of this glovebox is that it is a useful tool in training new scientists in fabrication techniques. The photolithography, Physical Vapor Deposition (PVD), and characterization tools in the glovebox are designed to be easy to use and thus afford new users a low-risk method of learning new techniques.

In chapter III we discuss a specific example of a new quantum phase of matter e.g. topological superconductivity in FTS. There, I discuss the fabrication requirements to probe this elusive phase as well as the unique measurement technique used to provide evidence that FTS is a higher-order topological superconductor. The characterization of FTS continues in Chapter IV where we reveal some exciting new results in the FTS system. These new results are direct evidence for the topological nature of FTS, a feat which has only been shown in Angle-Resolved Photo Emission Spectroscopy (ARPES) and Scanning Tunneling Microscopy (STM)

Chapter V concludes the dissertation with a summary of Chapters II, III, and IV. In addition, we give suggestions for future experiments to investigate the FTS system further as well as suggestions for insightful teaching programs with the cleanroom-in-a-glovebox.

## ACKNOWLEDGEMENTS

Ken.

Committee members.

Family.

LASE.

Collaborators.

Grad students.

Administrative staff.

Friends.

Pets.

Amanda.

Finish ac-  
knowl-  
edgements  
page

# TABLE OF CONTENTS

<b>ACKNOWLEDGEMENTS</b>	v
<b>LIST OF FIGURES</b>	viii
<b>LIST OF APPENDICES</b>	xi
<b>LIST OF ABBREVIATIONS</b>	xii
<b>CHAPTER</b>	
<b>I. Introduction</b>	1
1.1 Scope	1
1.2 New phases and particles	1
1.3 Topology and Superconductivity	1
<b>II. Cleanroom-in-a-Glovebox</b>	2
2.1 Introduction	2
2.2 Materials Characterization	5
2.3 Sample Fabrication	6
2.4 Ultra High Vacuum Suitcase	11
2.5 Conclusions	13
<b>III. Topology in <math>\text{FeTe}_{0.55}\text{Se}_{0.45}</math></b>	14
3.1 Introduction	14
3.2 Results and Discussion	19
<b>IV. New Results in <math>\text{FeTe}_{0.55}\text{Se}_{0.45}</math></b>	27
4.1 Introduction	27
4.2 Observation of Bias-Independent Conductance Plateau	28
4.3 Magnetic Field Dependence	29

4.4	Conclusion . . . . .	31
<b>V.</b>	<b>Conclusion . . . . .</b>	<b>33</b>
5.1	Summary . . . . .	33
5.2	Future Work . . . . .	34
5.2.1	Fe-based topological superconductivity . . . . .	34
<b>APPENDICES</b>	<b>. . . . .</b>	<b>36</b>
A.1	BTK Theory . . . . .	37
A.1.1	The Bogoliubov-de Gennes (BdG) Formalism . . .	38
A.1.2	The Blonder-Tinkham-Klapwijck (BTK) calculation . . . . .	40
A.2	Pseudo-Code for fitting spectra . . . . .	43
B.1	Measuring differential conductance . . . . .	49
B.2	Circuit construction . . . . .	50
B.2.1	Circuit troubles and solutions . . . . .	51
B.3	Three-point measurements . . . . .	53
<b>BIBLIOGRAPHY</b>	<b>. . . . .</b>	<b>54</b>



# LIST OF FIGURES

## Figure

2.1	1a) Picture of the Cleanroom-in-a-Glovebox. b) Raman spectra measured on $\alpha\text{RuCl}_3$ showing the difference exfoliation in the inert atmosphere makes. Raman measurements were taken using the WITec Raman System installed in the glovebox. c) $\text{Bi}_2\text{Sr}_2\text{CaCu}_2\text{O}_{8+\delta}$ exfoliated onto a thin film of $\text{Ga}_{1-x}\text{Mn}_x\text{As}$ . The film was then etched into a double hall-bar structure around the flake. d) Photo of the UHV suitcase during a device transfer from the glovebox to the low-temperature Raman system. The UHV suitcase is attached to the back of the glovebox. . . . .	4
2.2	a) Line scan using the <i>in-situ</i> AFM on a hafnium oxide and mica substrate. This data demonstrates both the effectiveness of our vibration isolation methods and the atomically flat surface of mica. b) Area scan of a patterned CVD graphene device using the <i>in-situ</i> Raman system. Graphene is outlined in green while color represents the intensity of the 2D-peak. c) Photoluminescence of $\text{MoS}_2$ exfoliated on mica. Blue data represents $\text{MoS}_2$ which was exfoliated onto mica in the glovebox while green represents exfoliation in the ambient environment. The inset shows Raman spectroscopy in the same conditions as the PL. We note that since the phonon modes do not shift in energy we can attribute this drastic change in PL to the inert glovebox environment and not to the dielectric characteristics of the substrate. . . . .	7

2.3	a) Photo taken when transferring a sample from the glovebox into the Low-temperature Raman system. Highlighted in green is the transfer arm from the UHV suitcase, in blue is the sample holder mounted onto the cryocooler, and in purple is the high NA Raman objective. b) Comparison of Raman spectra of GdTe <sub>3</sub> demonstrating the degradation of the sample when exposed to air for even a few minutes. c) Hall conductance versus Magnetic Field for a CVD grown graphene sample, fabricated into a hall bar geometry in the glovebox. Even at 7 K, the sample shows quantum oscillations (see arrows). d) Superconducting aluminum loops of 1 $\mu\text{m}$ radius fabricated onto FeTe <sub>0.55</sub> Se <sub>0.45</sub> demonstrating the single micron resolution of the $\mu\text{PG101}$ photolithography system. e) Periodic arrays of 1 $\mu\text{m}$ gold pillars. . . . .	10
3.1	a) Theoretical band structure of FeTe <sub>0.55</sub> Se <sub>0.45</sub> along the $\Gamma$ -Z and (b) the X- $\Gamma$ -M cuts[Wang2015]. The $p_z$ orbital of the chalcogenide is shown in blue, crossing the three d-orbitals, resulting in two Dirac points and topological, spin-orbit gap. c) Resistance vs. Temperature graph for an exfoliated flake of FTS, showing a clear superconducting transition around 10K. d) Diagram showing the ingredients needed for a Helical Majorana Hinge Mode . . . . .	16
3.2	a) False color image of the exfoliated device; numbers denote contacts used. b) $\frac{dI}{dV}$ vs DC Bias voltage for contact 5 at 7 K. c) $\frac{dI}{dV}$ vs DC Bias voltage for contact 3 at 7 K. d) Depiction of contact geometry for top only (5) and hinge (3) contacts. e) Dip number vs. Voltage for c-axis only contacts. The black line is a fit to McMillan-Rowell Oscillations which follow the equation, $\Delta V = n \times \frac{\hbar v_F}{4ed_s}$ . Blue and red points are experimental data extracted from the positive and negative bias voltages respectively. f) Temperature dependence of differential conductance for various temperatures. . . . .	19
3.3	a) $dI/dV$ versus voltage normalized to the spectra taken at $T_c$ (solid line) with a Lorentzian fit (dashed line), for $T = 7K, 9K$ , and $15K$ . b) and c) ZBCP heights and widths, respectively, extracted from the Lorentzian fit versus temperature. The exponential temperature dependence (orange lines) is at odds with a normal Andreev bound state that follows a $1/T$ dependence. The small energy scale of the exponential may result from the reduced superconducting gap on the side surfaces. While the rather small width at zero temperature is consistent with a topologically protected 1D mode. . . . .	23

3.4	a) Soft-point contact on a bulk crystal of FeSe normalized to the critical temperature. b) Differential conductance using a planar junction, revealing a similar zero-bias peak. The smaller height results from the normal resistance of the $\text{Bi}_2\text{Te}_2\text{Se}_1$ that is in series with the tunnel contact. c) Differential resistance versus scaled voltage (blue) plotted along with the resistance versus temperature curve (orange). The strong overshoot of the voltage-dependent resistance and its return at high-bias to the normal state resistance confirms the spectra and zero bias conductance peak are not a result of heating. . . . .	25
4.1	a) False color optical image of a representative device with a straight (100) edge. b) Tunneling Electron Microscopy (TEM) diffraction pattern demonstrating the (100) edge. Inset shows the flake measured as well as the diffraction aperture. c) Base temperature differential conductance curve. . . . .	29
4.2	Caption . . . . .	30
4.3	Caption . . . . .	32
A.1	Dispersion relations for a normal metal and superconductor in physical contact with one another. The red axis denotes the real-space position of the two materials with a potential barrier at their interface. The subset green, dashed axes denote the dispersion relations within the respective materials. A right-moving incident electron (top) can take one of four paths once it hits the NM/SC barrier: A) Andreev reflect as a left-moving hole, B) Normally reflect as a left-moving electron, C) Transmit as a right-moving electron-like quasi-particles, or D) Transmit as a right-moving hole-like quasi-particles. . . . .	41
A.2	Various demonstrations of the differential conductance calculated using the algorithms described in A.2. a) Single gap, zero Kelvin sweep of the potential barrier strength $Z$ . b) Single gap, zero Kelvin, zero barrier sweep of the thermal broadening parameter $\Gamma$ . c) Single gap, half-strength barrier, temperature sweep. d) Two superconducting gaps where the second gap is twice as large as the first demonstrating the $w$ parameter in action. . . . .	45
B.1	a) Circuit diagram to add AC and DC voltages then measure differential conductance as a function of applied DC bias. b) Voltage correction of data in Chapter IV via subtraction of extra measured voltage due to the system resistances along the way. c) Voltage correction of the same data by measuring the resulting current and multiplying it by the normal resistance. . . . .	52

# LIST OF APPENDICES

## Appendix

A.	Pseudocode for Andreev Reflection fitting . . . . .	37
1	Single Gap BTK conductance	442
	at finite temperature	463
	Fit	464
	BCS Gap	465
	Temperature Fit	47
B.	Model of the differential conductance circuit . . . . .	48

## LIST OF ABBREVIATIONS

**AR** Andreev Reflection

**DoS** Density of States

**STM** Scanning Tunneling Microscopy

**ARPES** Angle-Resolved Photoemission Spectroscopy

**PVD** Physical Vapor Deposition

**PAR** Perfect Andreev Reflection

**BTK** Blonder-Tinkham-Klapwijk

**LIA** Lock-In Amplifier

**BCS** Blonder-Tinkham-Klapwijk

**BdG** Bogoliubov-de Gennes

**ARPES** Angle-Resolved Photo Emission Spectroscopy

**FTS**  $\text{FeTe}_{0.45}\text{Se}_{0.55}$

**TEM** Tunneling Electron Microscopy

**hBN** hexagonal boron nitride

**TI** Topological Insulator

**PVD** Physical Vapor Deposition

# CHAPTER I

## Introduction

---

**1.1 Scope**

**1.2 New phases and particles**

**1.3 Topology and Superconductivity**

Write introduction on topology and fabrication.

# CHAPTER II

## Cleanroom-in-a-Glovebox

### 2.1 Introduction

Fabrication of devices at the nano-scale is central to future efforts in exploring novel quantum phases of matter and building next-generation devices. Previously this was achieved by creating dedicated facilities where the entire space is filtered and dust minimized via special air handling and attire for all who enter. While these cleanrooms minimize the amount of dust and other particles that can damage mesoscale devices, they do not protect the samples from either oxygen or water, at the same time they require extremely expensive and energy-intensive investments. In contrast, gloveboxes provide an inert atmosphere for working with oxygen and water sensitive materials, with greatly reduced initial and operational cost.[Chae2016] However, performing nanolithography in a glovebox risks contaminating the rest of the inert environment due to the various solvents involved. With these issues in mind, we've designed and constructed the cleanroom-in-a-glovebox to bridge the gap between these two approaches in order to prepare, fabricate, and characterize various scientific samples entirely within an inert argon atmosphere. The cleanroom-in-a-glovebox contains two separate work chambers where one chamber is devoted entirely to lithography and the other to prepara-

After writing proper intro, come back and make this flow.



tion and characterization (Fig. 2.1a). The system can be operated with minimal training, no need for special attire (i.e. gowning), and far fewer demands on the building. As such, the described cleanroom in a glovebox produces higher quality devices with air-sensitive materials, requiring far lower initial investment and operational cost than a traditional cleanroom. This makes the system described crucial in future efforts at training the quantum workforce and development of novel devices with a wider range of materials.

An overview of the system is shown in Fig. 2.1a, with the lithography chamber, (discussed in the “Fabrication” section), containing a Heidelberg  $\mu$ PG101 Direct-Write system, an Angstrom NexDep Thermal Deposition and Plasma Etching system, and a Spin-Coating Systems G3 Spin Coater. The characterization chamber contains a WITec alpha300R confocal Raman system (Fig. 2.1b & Fig. 2.2b), a Nanomagnetics ezAFM (Fig. 2.2a), a home-built 2D material dry-transfer system, electronic BNC and banana cable feedthroughs. These two chambers are connected via a small antechamber which allows us to transfer samples into and out of the gloveboxes while also enabling simple transfer between boxes without contamination. Lastly, attached to the back of the glovebox is an intermediate chamber for attaching a vacuum suitcase (Fig. 2.2d). This allows receiving from and transferring to a wide array of UHV systems, providing compatibility with electron-beam systems, scanning tunneling microscopy (STM), molecular beam epitaxy (MBE), angle resolved photoemission spectroscopy (ARPES) and other cutting edge tools. As such our processes and design enable a range of scientific tools on nanoscale, air-sensitive materials, while simultaneously reducing the time, training and cost involved.

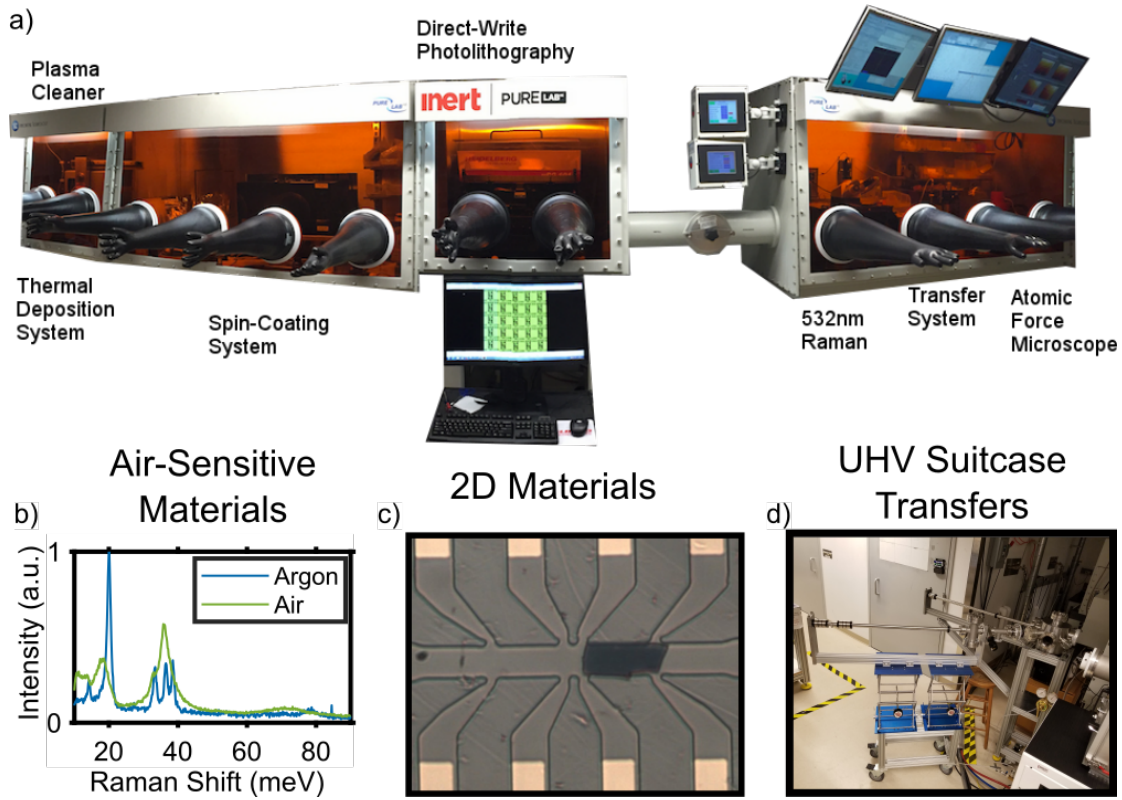


Figure 2.1: 1a) Picture of the Cleanroom-in-a-Glovebox. b) Raman spectra measured on  $\alpha\text{RuCl}_3$  showing the difference exfoliation in the inert atmosphere makes. Raman measurements were taken using the WITec Raman System installed in the glovebox. c)  $\text{Bi}_2\text{Sr}_2\text{CaCu}_2\text{O}_{8+\delta}$  exfoliated onto a thin film of  $\text{Ga}_{1-x}\text{Mn}_x\text{As}$ . The film was then etched into a double hall-bar structure around the flake. d) Photo of the UHV suitcase during a device transfer from the glovebox to the low-temperature Raman system. The UHV suitcase is attached to the back of the glovebox.

## 2.2 Materials Characterization

Atomic force microscopy (AFM) is an invaluable tool for characterizing materials. In the case of mesoscale physics, AFM is used to discern the thickness of exfoliated 2D materials. In other cases it characterizes the roughness of a substrate (such as in 2.2a) or sample. In order to resolve such small features, great care was taken to isolate the AFM system from environmental vibrations. This is more difficult than usual in a glovebox, as there are quite a few vibrations that arise from the gas-circulation system as well as sudden pressure changes from users inserting their hands into the glovebox to work on other tasks. To combat these vibrations the ezAFM and transfer stage were placed on a large granite slab. An additional Minus-K Vibration isolation stage was employed for the ezAFM and care was taken to ensure the cables were well secured to each other but did not touch the glovebox directly. The results of this are seen in Fig. 2.2a where we took an AFM scan of Mica, an atomically flat substrate. The noise levels of the scan are less than 5 angstroms in magnitude (the resolution of the ezAFM). To ensure rougher features can be resolved, this was compared with the AFM from HfO<sub>2</sub> film on a Si substrate grown by atomic-layer deposition. We note that ezAFM works with voice coils and thus is substantially less expensive and easier to use than a typical AFM system. Nonetheless, we anticipate a further reduction in noise with more traditional piezo-based scanning probes.

Raman spectroscopy can be used to tell the quality, doping level, thickness, symmetry, and cleanliness of samples.[**Ferrari:2013jx**, **Shahil:2010fg**, **Zhou2018**, **lei2019high**, **PhysRevB.82.064503**, **BTSAPLlocal2016**] For example, the ratio of the 2D peak to the G peak in graphene is commonly used to discern how disordered the sample is.[**wu2018raman**] With our Raman system's mapping capabilities, we determined the spatial distribution of the disorder after the fabrication of CVD graphene such as in Fig. 2.2b. The WITec system also allows

us to measure photoluminescence (PL) with a simple switch of energy ranges. PL is a useful measurement technique when working with materials such as MoS<sub>2</sub>, as it quickly identifies single-layer flakes, and provides insight into the interaction of MoS<sub>2</sub> with the substrate.[**YHlee2017review**, **yin2011single**, **Butler:2013ha**] We observed another advantage of the glovebox here. Namely, Mica is known to have charged potassium ions on the surface after cleaving but is quickly neutralized in air.[**Lui2009**] When exfoliating MoS<sub>2</sub> directly to the mica we found the PL consistent with the mica taking the MoS<sub>2</sub> from n-type to intrinsic.[**Mak2013**, **Ross2013**] (see Fig. 2.2c)

It is crucial to overcome the “glovebox-specific” problems to obtain the high-quality Raman and PL data. These are two-fold, first additional light contamination adding unwanted background signals and change in focus or position of the sample due to vibrations, air currents, and temperature fluctuations. To minimize these effects a simple casing was placed around the entire system, using black plastic sheets and 80-20 aluminum bars. Combined with careful isolation of the fibers and wires via foam sealing to the glovebox, the case enabled high-resolution Raman and PL area-scans like the one shown in Fig. 2.2b and c.

## 2.3 Sample Fabrication

The ability to create mesoscopic heterostructures has been crucial in the study of 2D materials, by enabling new physical effects and allowing encapsulation for removal to air.[**Dean:2012ht**, **Sharpe2019**, **Wu2018WTe2**, **stepanov2018long**, **Tang2017WTe2**, **Zareapour:2012ja**, **Island2019**, **Chae2016**] However, this relies on minimizing additional contaminants from solvents. Thus we constructed a standard dry-transfer system in the characterization chamber. To ensure excellent alignment and minimal drift during transfer, the stage was placed on a thick granite slab, with the required wires and tubing isolated from touching the glove-

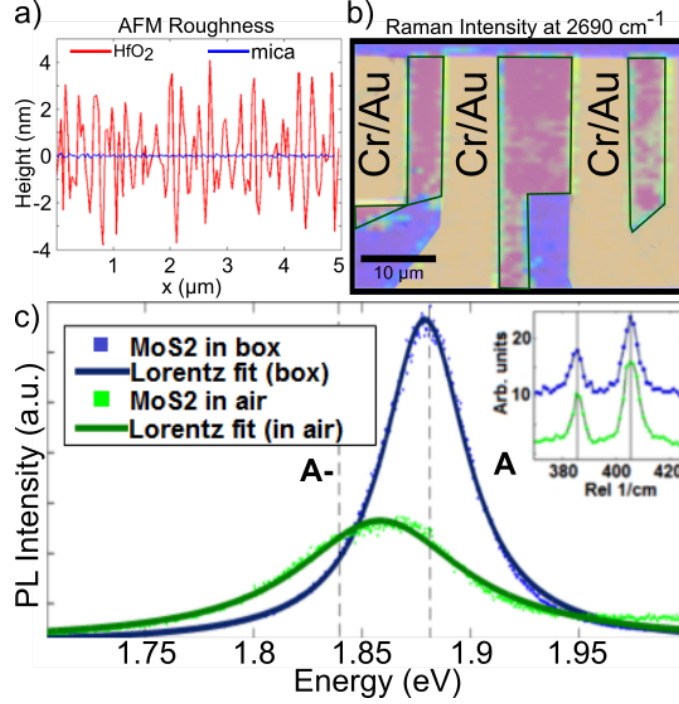


Figure 2.2: a) Line scan using the *in-situ* AFM on a hafnium oxide and mica substrate. This data demonstrates both the effectiveness of our vibration isolation methods and the atomically flat surface of mica. b) Area scan of a patterned CVD graphene device using the *in-situ* Raman system. Graphene is outlined in green while color represents the intensity of the 2D-peak. c) Photoluminescence of MoS<sub>2</sub> exfoliated on mica. Blue data represents MoS<sub>2</sub> which was exfoliated onto mica in the glovebox while green represents exfoliation in the ambient environment. The inset shows Raman spectroscopy in the same conditions as the PL. We note that since the phonon modes do not shift in energy we can attribute this drastic change in PL to the inert glovebox environment and not to the dielectric characteristics of the substrate.

box chamber directly. The transfer stage has six, fully-motorized stages, three of which are piezo-based Picomotor stages with a 30 nm step size providing precise positioning of the samples relative to one another, such as the heterostructure shown in Fig. 2.1c. Furthermore, this system has produced a number of complex devices including the realization of Coulomb Blockade into atomic defects in a 2D heterostructure[**Brotons-Gisbert2019**], observation of hinge modes in a higher order topological superconductor,[**Gray2019**] and CVD graphene sensors of bacteria with single cell resolution[**KUMAR2020112123**].

One of the key features of our cleanroom in a glovebox is our photolithography capabilities. In our fabrication chamber, we have an SCS G3 Spin Coater, Angstrom Engineering NexDep physical vapor deposition system, a UHV suitcase transfer system, and a Heidelberg  $\mu$ PG101 Direct-Write system. The glovebox column has a solvent scrubber installed, which allows for small amounts of solvent to be removed from the system. This keeps the rest of the environment clean while using the photolithographic, lift-off, and cleaning solvents. We employ the use of Qorpak bottles to limit the exposure of solvents to the glovebox atmosphere. These bottles have a PTFE liner in the caps that are resistant to most chemicals while also providing a low moisture transmission rate. In addition, we use activated charcoal as a passive solvent absorbent. Raman, PL, and AFM scans of materials before and after long term exposure to the fabrication chamber revealed no evidence for additional contamination. This is further attested to by our ability to observe quantum oscillations at relatively low fields in graphene devices fabricated inside (Fig. 2.3c).

The lack of contamination along with the alignment abilities of the mask-less system was crucial in creating high-quality devices and periodic structures (see Fig. 2.3d and 2.3e). The  $\mu$ PG101 has a resolution of 1  $\mu$ m with a 20 nm registry, optical auto-focus and can write up to a 5-inch wafer in one run. We note optical

auto-focusing is required as the changing dynamics of the glovebox air prevented the use of standard pressure alignment. The  $\mu$ PG101 stage runs on an air-bearing that is normally supplied with compressed air from the building, but this is not possible while in a glovebox as the unfiltered air would vent directly into the clean environment. Instead, we inserted a T-junction into the argon path from the cylinder where one side of the junction goes into the cylinder to supply the glovebox and the other supplies the stage with argon for the air-bearing. Not only does this solve the air-bearing problem but it also vents excess solvents and water from the clean atmosphere more quickly. To shut off the air-bearing when the system is not in use, we installed a cutoff valve after the T-junction that is shut when the stages don't need to move.

In a typical nanofabrication process, one must develop and dry the samples in air before moving them into a deposition tool. With an *in-situ* thermal deposition system glovebox users are able to develop and dry the sample in the inert argon environment before transferring them into the deposition tool. Furthermore, the deposition tool contains an *in-situ* plasma-cleaning system so samples can be de-scummed in high vacuum immediately before the deposition of metals. This step can be critical in establishing good electrical contact to certain materials. Following the deposition, small amounts of aluminum can be evaporated onto the samples followed by exposure to a 0.1% oxygen environment, creating an air-protection layer of alumina.[**Damasco2019tunnel**] This layer of alumina can also be used to protect samples against photoresists during nanofabrication processes as it is easily removed by TMAH-based developers. For example, when fabricating CVD graphene devices we first deposit a layer of alumina before spin-coating photoresists while the rest of the fabrication process remains exactly the same, including energy dosage and developing times. The areas of photoresist that are developed out also allow for the developer to come in contact with the alu-

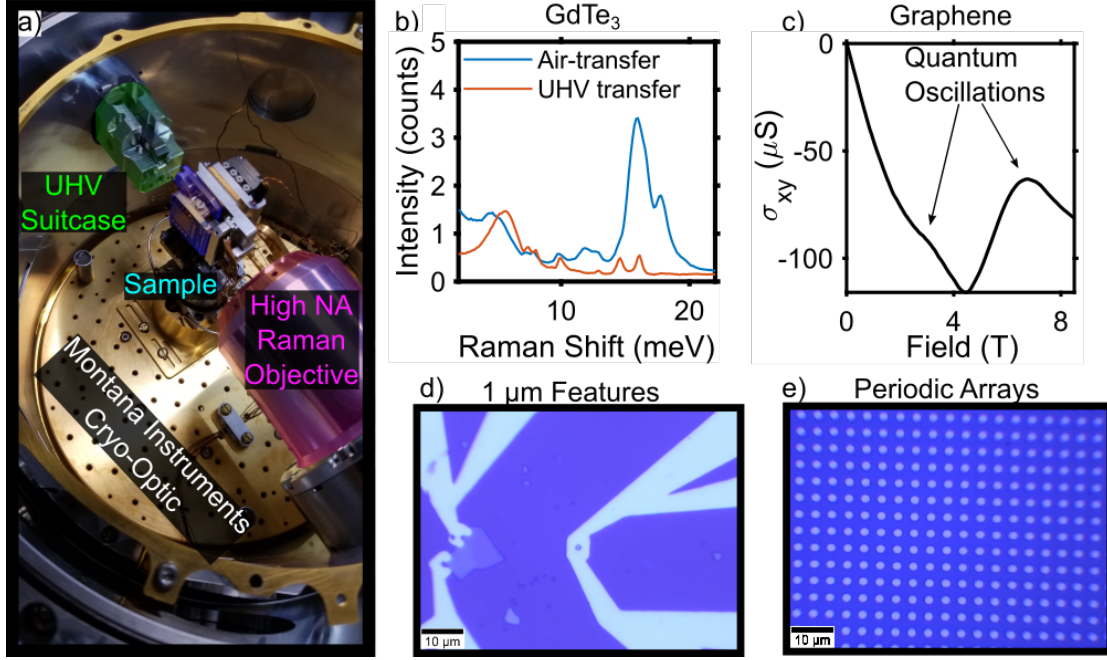


Figure 2.3:

a) Photo taken when transferring a sample from the glovebox into the Low-temperature Raman system. Highlighted in green is the transfer arm from the UHV suitcase, in blue is the sample holder mounted onto the cryocooler, and in purple is the high NA Raman objective. b) Comparison of Raman spectra of  $\text{GdTe}_3$  demonstrating the degradation of the sample when exposed to air for even a few minutes. c) Hall conductance versus Magnetic Field for a CVD grown graphene sample, fabricated into a hall bar geometry in the glovebox. Even at 7 K, the sample shows quantum oscillations (see arrows). d) Superconducting aluminum loops of 1  $\mu\text{m}$  radius fabricated onto  $\text{FeTe}_{0.55}\text{Se}_{0.45}$  demonstrating the single micron resolution of the  $\mu\text{PG101}$  photolithography system. e) Periodic arrays of 1  $\mu\text{m}$  gold pillars.



mina, removing it as well. Thus we are still able to make good electrical contact to the graphene while preventing contact with the photoresist and other potential dopants.

The deposition tool also opens to the outside allowing users to clean samples with argon plasma or thermal annealing before loading them into the glovebox. An example is our fabrication of CVD graphene devices for use in bio-sensing applications. The CVD graphene is grown on copper foil and thus must be transferred onto SiO<sub>2</sub>/Si wafers via wet transfer.[doi:10.1021/acs.nano.6b04110] In order to clean the graphene, we bake the samples in the deposition tool at 350 °C in 10<sup>-7</sup> mBar pressure for nine hours before alumina deposition (described above) then subsequently transferring samples into the glovebox for patterning. The result of this is samples that are clean enough to not only see quantum oscillations at 8 K and 7 T shown in Fig. 2.3c, but are also able to be used as single-bacterium bio-detectors.[KUMAR2020112123]

## 2.4 Ultra High Vacuum Suitcase

After fabrication, samples typically must be taken out of the glovebox to be measured in more specialized pieces of equipment such as surface-sensitive (STM, APRES) or low-temperature transport and optical probes. Furthermore, many new materials and heterostructures are first created by MBE, requiring *in-situ* probes to determine their device characteristics.[Gerber2017FeSe, Wang2016, Hellman2017Rev] This presents a chance for the samples to see air and degrade. Typically this is avoided by coating the samples with a “capping-layer” (e.g. alumina) or covering mesoscale samples with hBN. However, samples may interact with these materials in unexpected ways such as accidental electrical shorting if the alumina contains many pinholes or if the hBN induces strain into the samples. The addition of hBN to an exfoliated flake could cause additional complexities

including changing the dielectric environment or inducing Moire patterns that, while exciting, make reproducibility of devices quite difficult as both layers must be aligned in the same orientation for every device.[**Sharpe2019**, **Woods2014**, **doi:10.1021/nl5006542**, **Tran:2019aa**, **Jin:2019aa**, **Alexeev:2019aa**, **Yankowitz2019**, **Cao2018**] Another exciting example of eliminating hBN from air-sensitive devices is the  $\beta$ -Fe<sub>1.1</sub>Se crystal, where recent experiments have shown enhancements of  $T_c$  in monolayer films as compared to bulk samples but clean monolayer-devices have yet to be realized.[**Gerber2017FeSe**, **Wang2016**] This is in part due to the air-sensitivity of the system at low layer numbers but is also due to the crystal's sensitivity to strain.[**Yang2019**] Recent experiments have shown that the  $T_c$  of  $\beta$ -Fe<sub>1.1</sub>Se thin films change as much as 10 K with 1% strain which demonstrates the problem in making hBN encapsulated devices.[**Kawai2018**]

To expand the range of probes and fabrication capabilities of the cleanroom-in-a-glovebox, we designed and built a UHV chamber to couple to various vacuum suitcases (see Fig. 2.1d). The intermediate chamber has a block for attaching different kinds of sample holders allowing us to transfer materials into the glovebox from MBE and out to STM, low-temperature Raman, or electrical transport systems (e.g. see Fig. 2.3a). One measurement system of particular interest is the custom-designed Montana Instruments low-temperature Raman system. This system has been described in detail in other works[**Tian2016**] but has been adapted to be compatible with a UHV suitcase. All of the suitcases that are used follow typical transfer procedures with the addition of a connection to an inlet for Argon gas. Specifically, after the sample is brought into the intermediate space, the suitcase is valved off and Ar added to bring the chamber to match the glovebox pressure. Once matched the intermediate chamber is opened to the glovebox, where the sample holder is brought in using a second manipulator arm. When transferring devices out of the glovebox a baking step is added to the normal pro-

cess after vacuuming where the entire chamber is heated to 120°C. This step helps remove any excess impurities introduced when exposing the intermediate chamber to the glovebox.

The merits of such work are shown in Fig. 2.3b, where we probe the Raman response of  $\text{GdTe}_3$ , established to be highly air sensitive.[lei2019high] Two bulk crystals were prepared in the glovebox, then one was transferred into the low-temperature Raman system in air and freshly cleaved just before cool down. The second sample was transferred via the UHV suitcase. The crystal that was transferred in air clearly shows a large tellurium oxide peak around 17 meV that obscures phonon modes.[YaoCGT2Dmat, lei2019high] However, the material transferred via vacuum suitcase revealed sharp phonon modes, with the exception of the CDW amplitude mode at low energies. In addition, we found the Raman response to be much more uniform across the sample surface.

## 2.5 Conclusions

Here we demonstrated the construction and operation of a cleanroom-in-a-glovebox. The system combines the inert environment of a glovebox with the fabrication and characterization facilities of a cleanroom. While modifications had to be made to existing equipment and procedures, the result is a fast and efficient fabrication facility that allows devices made from many air-sensitive systems that were previously unattainable. In addition, the far reduced cost, ease of use, and environmental requirements open the door to using this setup in a wider array of educational as well as research settings.

## CHAPTER III

# Topology in $\text{FeTe}_{0.55}\text{Se}_{0.45}$

### 3.1 Introduction

New particles can be a convincing signature of emergent phases of matter, from spinons in quantum spin liquids[Balents2010] to the Fermi arcs of Weyl semimetals[Armitage2017, Zhang2019]. Beyond potentially indicating a broken symmetry or topological invariant, they can be put to use in future topological quantum computers[Nayak2008]. Until recently it was believed the non-trivial topology of the bulk would lead to new states in one lower dimension at the boundary with a system of differing topology. However, higher order topological insulators (HOTI) have been realized[Schindler2018, Ni2018, Xue2019, Song2017, Langbehn2017, Benalcazar2017], where the resulting boundary modes exist only at the intersection of two or more edges, producing 1D hinge or 0D bound states. One route to creating these higher order states is through the combination of a topological insulator and a superconductor with anisotropic pairing[Wang2018Corner, DasSarma2018, Zhongbo2018, Ghorashi2019]. Usually, this is done by combining two separate materials and inducing superconductivity into the TI via proximity[Zareapour2012, Albrecht2016, Gazibegovic2017, Kurter2018, Tanaka2012]. However, this method requires long coherence lengths

After  
edits to  
Chapter 2,  
come back  
and make  
this flow.

and extremely clean interfaces, making experimental realization of devices quite difficult. For studying HOTI, as well as the combination of strong correlations and topology, the material  $\text{FeTe}_{0.55}\text{Se}_{0.45}$  (FTS) may be ideal, as it is a bulk, high-temperature superconductor with anisotropic pairing that also hosts topologically non-trivial surface states[Zhang2018, Wang2015, Wang2018].

FTS is part of the  $\text{FeTe}_{1-x}\text{Se}_x$  family of Fe-based superconductors, which ranges from an antiferromagnet in FeTe to a bulk superconductor in FeSe[Liu2010]. These generally have the same Fermiology as the other Fe-based superconductors in that there are hole pockets at the  $\Gamma$ -point and electron pockets at the M-points[Homes2015, Hanaguri2010, Miao2012, Okazaki2012, Zhang2018]. The relative strengths of the interband vs intraband scattering in principle should determine the superconducting symmetry, however, there is a complex interplay between the spin-fluctuation exchange, intraband Coulomb repulsion, and the doping level that all contribute to the symmetry of the superconducting order parameter[Kreisel2016, Chubukov2012]. Indeed, experiments performed on  $\text{FeTe}_{0.55}\text{Se}_{0.45}$  find no evidence for a node with strong signatures of  $s^\pm$  order,[Hanaguri2010, Miao2012, Zeng2010] while experiments on other alloys suggest nodal  $s^\pm$ , anisotropic s-wave, and even p-wave[Michioka2010, Serafin2010, Bendele2010, Kim2010, Okazaki2012]. Interestingly, tuning away from FeSe leads to enhanced spin-orbit coupling and bandwidth. As a result, the p-orbital is shifted down in energy, crossing the d-orbitals with opposite parity along the  $\Gamma$  to  $Z$  direction (See Figure 3.1a and b). The first two crossings are protected by crystalline-symmetry resulting in bulk Dirac states above the Fermi energy. However, the lowest energy crossing is avoided resulting in a spin-orbit coupled gap, resembling those typically found in topological insulators[Wang2015, Chen178]. While the Fermi level falls into this gap, the original hole and electron Fermi surfaces at  $\Gamma$  and  $M$ , respectively, are retained[Zhang2018, Wang2015]. ARPES measurements have

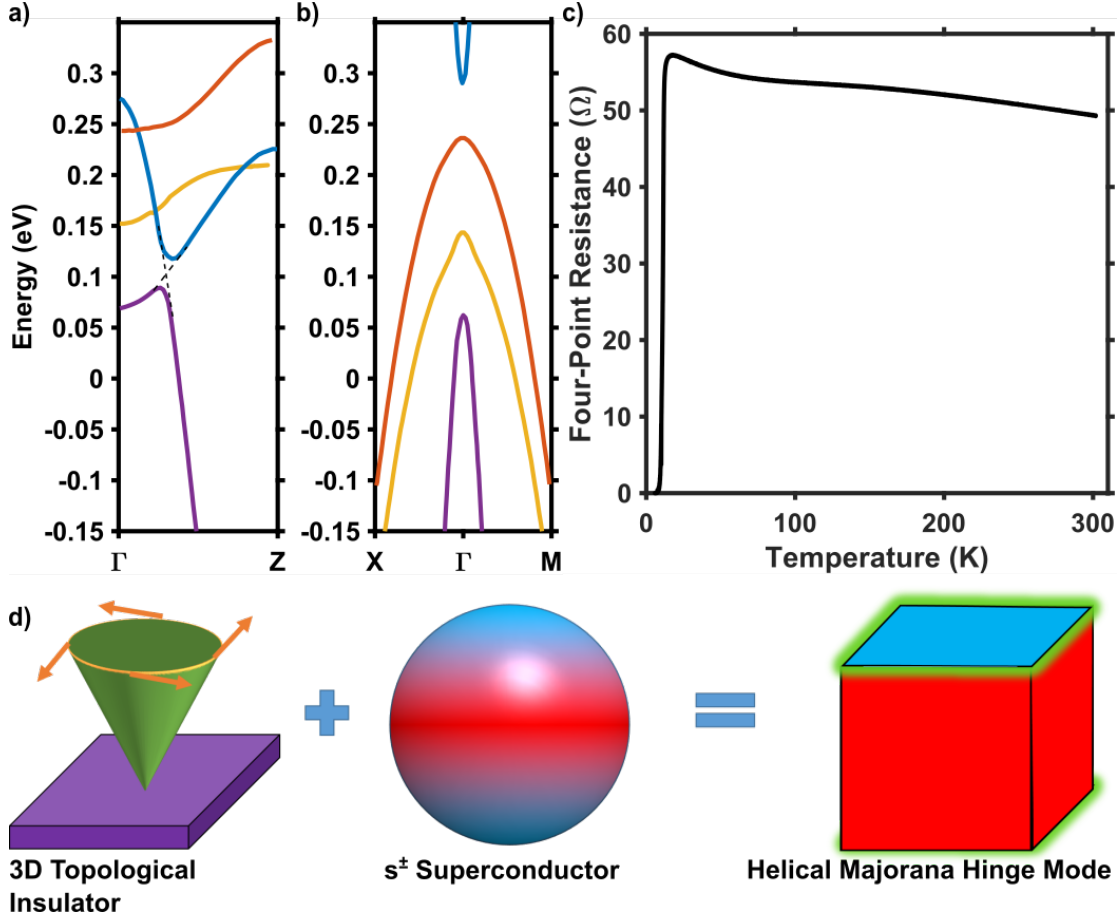


Figure 3.1: a) Theoretical band structure of FeTe<sub>0.55</sub>Se<sub>0.45</sub> along the  $\Gamma$ -Z and (b) the X- $\Gamma$ -M cuts[Wang2015]. The  $p_z$  orbital of the chalcogenide is shown in blue, crossing the three d-orbitals, resulting in two Dirac points and topological, spin-orbit gap. c) Resistance vs. Temperature graph for an exfoliated flake of FTS, showing a clear superconducting transition around 10K. d) Diagram showing the ingredients needed for a Helical Majorana Hinge Mode

observed the resulting spin-momentum locked surface states, as well as their gapping out in the superconducting state[Zhang2018, Zhang20192]. Additionally, there is evidence from STM that this results in apparent Majorana zero-modes inside magnetic vortices[Wang2018, Dong-LaiFeng2018, Machida2018].

Recent theoretical work on FTS has suggested that the combination of an  $s^\pm$  order parameter and topological surface states could give rise to higher order topological superconductivity[DasSarma2018]. In short, the changing superconducting phase causes the surface states to gap out anisotropically. Depending on the relative strength of the isotropic versus the anisotropic term, this could lead to the [001] and the [100] or [010] face having superconducting order parameters with opposite phase. As shown in Figure 3.1d), this is predicted to produce a pair of 1D Helical Majorana Hinge Modes emerging at the 1D interface of the top/side surfaces[DasSarma2018]. Whether or not the modes we observe are indeed Majorana modes, the appearance of HHZM requires both  $s^\pm$  superconductivity as well as strong 3D TI surface states. Thus observing Helical Hinge Zero Modes in FTS would provide strong evidence that it is an  $s^\pm$  topological superconductor.

To search for the HHZM it is tempting to rely on methods previously exploited to reveal the unconventional nature of the cuprates[Deutscher2005]. Specifically, normal-metal/superconductor junctions demonstrated Andreev Bound States resulting from the d-wave order only on [110] surfaces[Tanaka2003, Sinha1998, Greene1999, Tanaka2012]. In the case of FTS, this approach is more challenging as one must tunnel into the hinge between [001] and [010] and the modes are nominally charge neutral, thus requiring an Andreev process to be observed[zhang2017quantum]. To achieve this, we created 2D atomic crystal heterostructures with thick hBN covering half of the FTS. By draping contacts over the side of the FTS or atop the hBN we can separately probe conductance into the hinge from the c-axis. As expected for modes protected from back-scattering, we find a cusp-like zero-bias

peak only on the hinge contacts that is absent from the c-axis junctions. The mode is well-described by a Lorentzian, consistent with other studies on one-dimensional zero-energy bound states[**Setiawan2017**]. Confirmation that the mode does not result from our fabrication method or defect density is provided by soft-point contact measurements on facets of various bulk crystals (See Supplemental Fig S3). Taken together these data strongly suggest the presence of the HHZM in FTS resulting from its higher order topological nature and the presence of  $s^\pm$  superconductivity[**Park:2010wo**, **Tanaka2012**]. The helical hinge zero mode in FTS should only exist in the superconducting state. As such we expect a sharp zero-bias conductance feature below  $T_c$  on the hinges between the [001] and side surfaces as compared to purely on the [001] face. Alternatively, Majorana zero modes on the hinge should give quantized conductance, revealed through nearly perfect Andreev reflection.[**DasSarma2018**] However, as discussed later, observing this quantized conductance may be challenging as the coherence length in FTS is  $\approx 3nm$ [**Kim2010**, **Bendele2010**]. To test this we used 2D atomic crystal heterostructures to simultaneously fabricate Normal Metal/Superconductor (NS) low-barrier junctions on various crystal facets (See Figure 3.2a and 3.2d). The first type of NS junction is a standard lithographically-defined contact that drapes over the edge of the exfoliated flake. This contact will form a junction with the [001] and [100] surfaces as well as the hinge between them. The second type of contact is fabricated by first transferring hexagonal Boron Nitride (hBN) over half of the FTS flake, insulating the side and edge from electrical contact. We then drape a contact over the side of the hBN, forming a junction primarily on the [001] face (See depiction of the side view in Fig 3.2d). The entire fabrication process, from exfoliation to device, is performed in an inert argon atmosphere or vacuum. Patterns for mesoscale contacts were defined using standard photolithography techniques and our Heidelberg  $\mu$ PG101 direct-write lithography system. Contact areas are



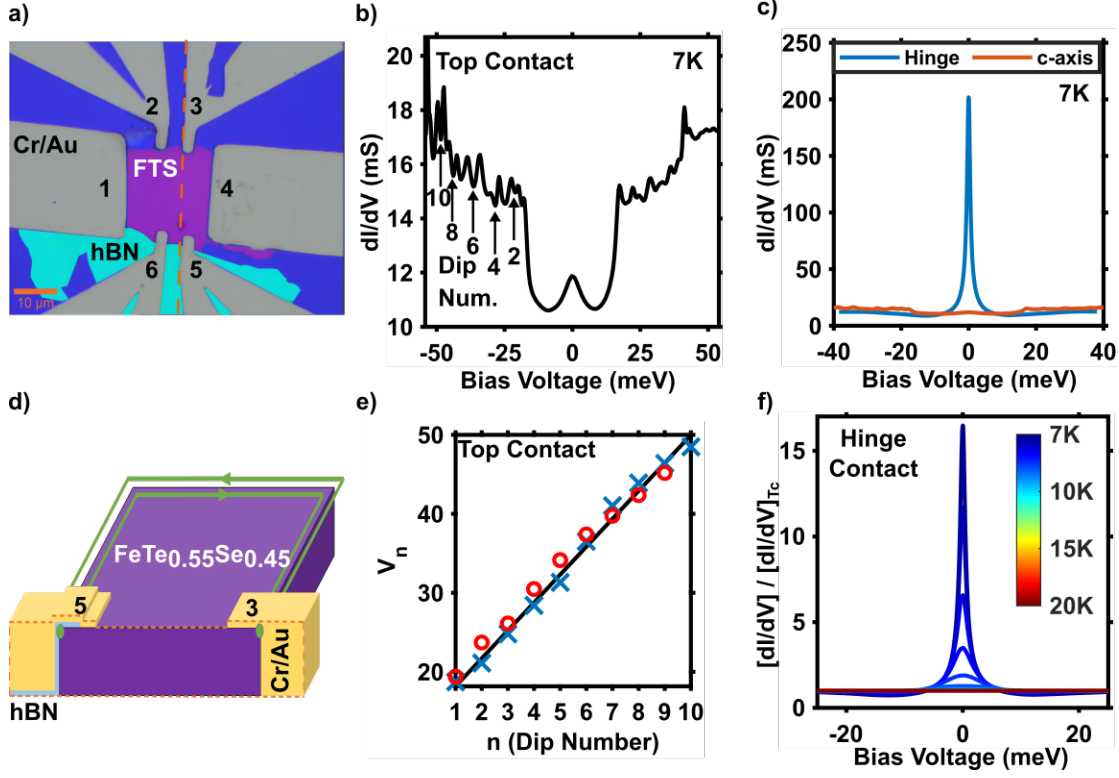


Figure 3.2:

a) False color image of the exfoliated device; numbers denote contacts used. b)  $\frac{dI}{dV}$  vs DC Bias voltage for contact 5 at 7 K. c)  $\frac{dI}{dV}$  vs DC Bias voltage for contact 3 at 7 K. d) Depiction of contact geometry for top only (5) and hinge (3) contacts. e) Dip number vs. Voltage for c-axis only contacts. The black line is a fit to McMillan-Rowell Oscillations which follow the equation,  $\Delta V = n \times \frac{h\nu_F}{4ed_s}$ . Blue and red points are experimental data extracted from the positive and negative bias voltages respectively. f) Temperature dependence of differential conductance for various temperatures.

then cleaned with an argon plasma at high vacuum immediately before thermal deposition of 5nm of Cr then 45nm of Au. Full fabrication details can be found in the Supplementary.

### 3.2 Results and Discussion

We first established that our control contacts are only tunneling into the c-axis by studying their base temperature differential conductance. Specifically, we

sourced current between a top contact (5 or 6 in Fig. 3.2a) to one of the current leads (#1 or #4), while measuring the resulting voltage between the same top contact and the other current contact. This three-point experiment ensures the conductance results primarily from the interface of the top contact. As shown in Fig 3.2b, we observe a small zero bias conductance peak that is  $\approx 20\%$  higher than the background. The shape and height are consistent with previous point contact Andreev reflection measurements along the c-axis of  $\text{FeTe}_{0.55}\text{Se}_{0.45}$ , [Daghero2014] and confirms the contacts are in the low-bias, Andreev regime. We note these previous works were performed at temperatures below our base temperature, and as such could resolve the rather small gap. At higher bias, we observe an enhancement in the conductance at  $|V| \geq 20 \text{ meV}$ , consistent with spin-orbit induced gap. Above this value, we observe a series of conductance dips that are fully consistent with McMillan-Rowell Oscillations (MRO) [2004PhyC..408..618C, 2004PhRvB..69m2507S]. These MRO result from Fabry-Perot like interference of quasiparticles in the normal layer undergoing AR at the interface and reflecting off the back surface of the metal. The MRO are linearly spaced by voltages [2004PhyC..408..618C] defined by the equation  $\Delta(V) = n \cdot \frac{ev_F}{hd}$  where  $n$  is the dip number,  $v_F$  is the Fermi velocity at the contact, and  $d$  is the thickness of the metal which we set to 50 nm (See Figure 2e). From this fit, we extract a renormalized Fermi velocity of approximately  $1.7 \times 10^5 \text{ m/s}$ . We note that similar behavior was observed if the current/Voltage was reversed between contacts #1 & #4, we measure from contact #6, or measuring between contacts #6 and #5 exclusively (see Supplemental Fig S4a). This shows the robustness of these results and combined with the detailed spectra, confirm the contacts over the hBN are Andreev tunneling only into the c-axis.

Next, we turn to the spectra measured in an identical manner, but with the hinge contact (#3 in Fig. 3.2a). Since the normal-state and high bias resistance of

the hinge contact is nearly identical to the control contact we expect the spectra to be similar. However, as shown in Fig. 3.2c the zero-bias conductance in the hinge contact is quite distinct from the response observed in the control contact and previous point contact experiments. Specifically, we observe a cusp-like zero-bias conductance peak (ZBCP) in the hinge contact that reaches a value 17-times higher than the high bias or  $T \approx T_c$  conductance. This rather large enhancement is also likely responsible for the absence of a clear observation of the gap, which would be far smaller. These results provide strong evidence for a zero mode that only exists on the hinge. The "cusp-like" shape and magnitude of the peak could result from an Andreev Bound State (ABS)[**Deutscher2005**, **Sinha1998**, **Greene1999**], however, this requires either a node in the superconducting gap or time-reversal symmetry breaking,[**Yakovenko2002**, **TanakaTopSym2012**] neither of which has been detected in  $\text{FeTe}_{0.55}\text{Se}_{0.45}$ [**Serafin2010**, **Zeng2010**, **Bendele2010**, **Okazaki2012**, **Miao2012**, **Kim2010**, **Hanaguri2010**]. As discussed later, direct evidence against the ABS interpretation is provided by the dependence of the peak on temperature, and near independence on the contact's type (planar, point contact) or material (Ag, Au,  $\text{Bi}_2\text{Te}_2\text{Se}_1$ ). Interestingly, this behavior is also inconsistent with previous observations of standard Andreev Reflection(AR)[**Tanaka2003**], Coherent Andreev Reflection (CAR)[**Klapwijk1992**], the Kondo Effect[**Sasaki2000**, **Samokhin2001**], and Joule heating[**Naidyuk2018**].

To ensure the zero bias conductance peak emerges at  $T_c$  and is not the result of an ABS, we directly analyzed its temperature dependence by fitting the data with a Lorentzian line shape. This is based on recent theoretical studies on one-dimensional superconducting wires showing that both Majorana Zero Modes and ABS produce a Lorentzian differential conductance spectra[**Setiawan2017**]. While this may not be the correct model for our case, to the best of our knowledge there are no calculations for the conductance spectra expected from hinge

modes in a higher order topological superconductor. Nonetheless, the differential conductance spectra are generally well described by a Lorentzian (see Fig 3.3a). The temperature dependence of the height and width of the peak determined by the fits for the data presented in Fig. 3.2f are shown in Fig. 3.3b & c, respectively. These data provide direct evidence for the connection to the bulk superconductivity, though are inconsistent with an ABS. Indeed, we find that as the temperature is raised, the height of the ZBCP decreases exponentially until it is completely quenched at  $T_c$  (see Fig3.2a and Fig3.3b), where we define  $T_C$  as the temperature for which  $\frac{dR}{dT}$  passes through zero. While lower temperature data are required to determine the exact functional form, it is clear from Fig. 3.3b & c that the mode is substantially different from the  $1/T$  behavior typically expected from an ABS. Furthermore, we found a similar shape and temperature dependence in contacts of various barrier height, also inconsistent with standard Andreev reflection.[**BTK, Tanaka2012, Lofwander2001**]

Similar to the height of the peak, we find the width of the zero bias conductance peak grows exponentially with temperature (see Fig. 3.3). Interestingly the energy scale governing the peak height ( $E_H \approx 0.08 \text{ meV}$ ) and the width ( $E_T \approx 0.1 \text{ meV}$ ) are quite close. We note that comparable results were obtained from other contacts revealing the hinge mode. Nonetheless, the energy scales governing the temperature dependence of the mode are far smaller than either the superconducting gap of the bulk or the surface states.[**Zhang2018**] However, to the best of our knowledge, the size of the superconducting gap on the side surface has not been measured. As such we speculate this small apparent energy scale results from a much weaker proximity effect on the [010] and [100] surface states. Interestingly, extrapolating the width of the zero bias peak to zero temperature suggests an extremely narrow mode ( $\approx 3.5 \text{ } \mu\text{eV}$ ). While further studies at lower temperatures are required to confirm this extrapolation and the specific shape of

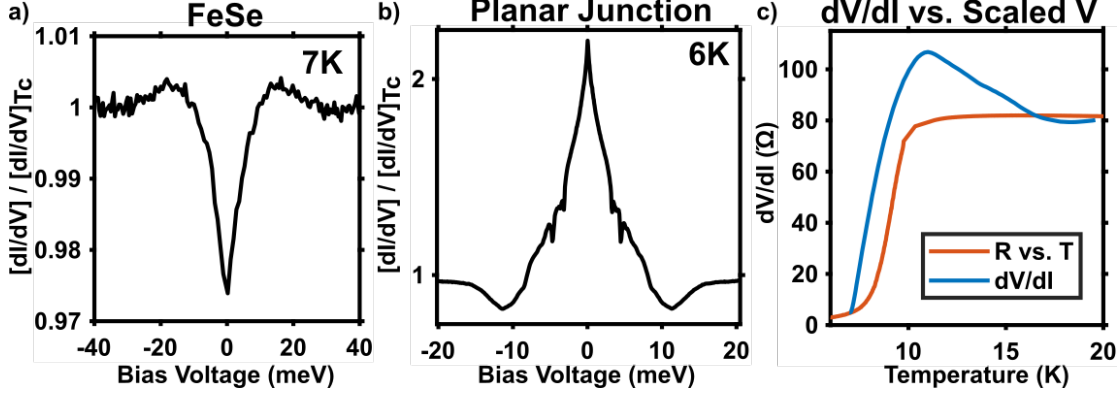


Figure 3.3:

a)  $dI/dV$  versus voltage normalized to the spectra taken at  $T_c$  (solid line) with a Lorentzian fit (dashed line), for  $T = 7K, 9K$ , and  $15K$ . b) and c) ZBCP heights and widths, respectively, extracted from the Lorentzian fit versus temperature. The exponential temperature dependence (orange lines) is at odds with a normal Andreev bound state that follows a  $1/T$  dependence. The small energy scale of the exponential may result from the reduced superconducting gap on the side surfaces. While the rather small width at zero temperature is consistent with a topologically protected 1D mode.

the mode, if correct it points to the highly coherent nature of the excitation. As such the temperature dependence is consistent with our expectations for topologically protected 1D modes.

For additional confirmation that the ZBCP does not result from fabrication, exfoliation, impurities or the specific metal used in the contact, we performed a series of additional control experiments, summarized in Fig (3.4). First, the topological gap in FTS closes with reduced tellurium levels, thus we expect the hinge mode is absent from FeSe. To confirm this as well as the irrelevance of contact type or normal metal used, we employed soft-point contact measurements. For FeSe we observe no evidence of an increase in conductance at zero bias below  $T_c$  (see Fig (3.4a)). However, performing the same soft-point contact spectroscopy across multiple different  $FeTe_{0.55}Se_{0.45}$  crystals always produces an increase in conductance at zero-bias when cooled below  $T_c$  consistent with the data on contacts made via photolithography (see Supplemental Fig S3). The soft-point contacts

revealed a smaller enhancement of the zero bias conductance in the superconducting state. However this is expected since the quasi-particle lifetime in the Ag point contact is likely lower, which smears the spectra and reduces the height at zero bias. Similarly, we used planar junctions with  $\text{Bi}_2\text{Te}_2\text{Se}_1$  via a method that has previously enabled spectroscopic studies with low barriers in van der Waals materials.[Zareapour2012] As shown in Fig. 3.4b, these junctions also resulted in nearly identical spectra near zero bias. Here the lower zero bias conductance is expected as it contains contributions from the normal material being in series with the contact. Another extrinsic explanation for the peak is the interstitial Fe-atoms known to be present in these materials. However, we excluded this explanation by measurements on annealed samples where the Fe impurity content is dramatically reduced (see Supplemental Fig S3a), though the topology and  $T_c$  are only mildly affected.

An alternate mechanism for producing a ZBCP is Joule heating at the contact. We took a number of steps to rule this out. First, similar results were obtained regardless of the exact contact configuration (e.g. swapping contacts employed for current versus voltage in point contact or three-point measurements). In addition, we compared the voltage and temperature data by inverting the  $\frac{dI}{dV}$  spectra and comparing it to the resistance versus temperature data taken on the same contact configuration (see Fig 3.4c). To align the two curves, we translate the  $\frac{dV}{dI}$  curve such that zero voltage coincides with the temperature at which it was recorded (7 K). Next, we assume the voltage where the maximum resistance is measured is equivalent to heating to  $T_C$ , as this is the temperature where a peak in resistance is typically observed (see Fig 3.1d). While the exact voltage dependence due to heating could be more complex, it is clear the  $\frac{dV}{dI}$  versus voltage spectra are far in excess of the resistance measured at  $T_c$ , though at high bias they do return to the value measured at  $T_c$ . This further excludes voltage induced heating as the origin

of the zero bias conductance peak. In addition, the background conductances in the c-axis, hinge, and point contacts are nearly identical. Therefore the heating across all of them should be approximately the same. However, they reveal quite distinct spectra (i.e. strong ZBCP in the hinge contact vs. nearly none in the c-axis) which, combined with the emergence of the zero-bias conductance peak (ZBCP) at  $T_c$  in numerous contacts (see Figure 3.2 and Supplemental Figure S2), eliminates heating.

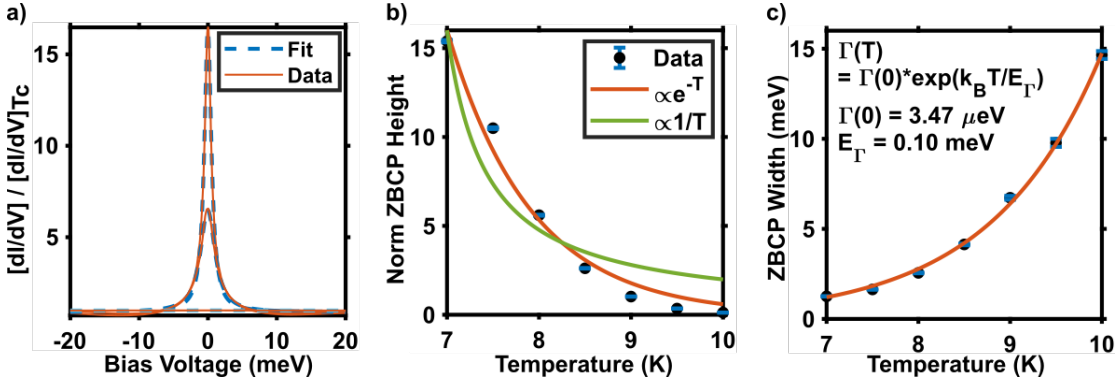


Figure 3.4:

a) Soft-point contact on a bulk crystal of FeSe normalized to the critical temperature. b) Differential conductance using a planar junction, revealing a similar zero-bias peak. The smaller height results from the normal resistance of the  $\text{Bi}_2\text{Te}_2\text{Se}_1$  that is in series with the tunnel contact. c) Differential resistance versus scaled voltage (blue) plotted along with the resistance versus temperature curve (orange). The strong overshoot of the voltage-dependent resistance and its return at high-bias to the normal state resistance confirms the spectra and zero bias conductance peak are not a result of heating.

In summary, via a variety of contact methods, we reveal helical hinge zero modes in the topological superconductor  $\text{FeTe}_{0.55}\text{Se}_{0.45}$ . Specifically, contacts to the  $[001]$  surface made using hBN reveal standard Andreev reflection, while those draped over the hinge contain a cusp-like, zero-energy feature in the differential conductance. By combining with measurements using soft-point contacts on various crystals, we further confirm the intrinsic nature of this new mode. Furthermore, the appearance of an HHZM in FTS helps to establish both the topological

and  $s^\pm$  nature of the superconductivity. An important question raised by these results is the large size and the temperature dependence of the HHZM. It is possible that the large ratio of contact area to coherence length at the measured temperature ( $\approx 1000x$ ), makes the measurement essentially many point-like contacts in parallel, leading to an apparently large conductance. The contact size may also play a role in the temperature dependence, as could the unknown size of the superconducting gap on the side surface. Thus future theoretical and experimental efforts must be made to better separate out the contact effects from the intrinsic response of the hinge mode we observe.



## CHAPTER IV

### New Results in $\text{FeTe}_{0.55}\text{Se}_{0.45}$

#### 4.1 Introduction

Using a control contact draped over hexagonal boron nitride (hBN) we demonstrated strong evidence for a normal mode on that exists purely on the hinge or side of the FTS crystal[Gray2019]. Recent works have called into question the exact topological nature of FTS claiming the crystal is not a topological insulator but rather a topological semi-metal with buried Dirac nodes. In light of this it is crucial to obtain evidence with more experimental techniques to better understand the nature of the topology in the FTS system. Indeed, the underlying physics which predicts the helical hinge mode also predicts the same mode to manifest as a bias-independent conductance plateau in a differential conductance measurement rather than the previously observed zero-bias conductance peak. To accomplish this, we investigate the effect edge quality has on the topological characteristics of FTS as it has been previously shown that the quality of the crystal edge can have a drastic effect on its transport characteristics . We find that when tunneling measurements are performed across pristine, high-symmetry crystalline edges bias-independent conductance plateaus are observed for biases below the superconducting gap energy while “rough” edges do not exhibit such plateaus.

Write exciting new results in FTS along with questions left to verify.

cite Andrea's work on different transport characteristics of

Furthermore, these plateaus are consistent with Perfect Andreev Reflection.

## 4.2 Observation of Bias-Independent Conductance Plateau

The tunneling conductance of a normal-metal/superconductor interface can be modeled by assuming an delta-function potential barrier at the interface characterized by a strength parameter  $Z$ , i.e., the BTK method. An in-depth discussion and pseudo code for performing these simulations can be found in A], however we will take some of the main results of these calculations for discussions here. The BTK method on a standard Blonder-Tinkham-Klapwijk (BCS) s-wave superconductor predicts a bias-independent conductance plateau only when the strength of the potential barrier between the normal-metal and superconductor is exactly zero. Even slight deviations from a zero-strength barrier result in significant dips around zero-bias, thus observing Perfect Andreev Reflection (PAR) is exceedingly rare and typically only occurs only in extremely clean materials . Therefore when PAR is observed in a system it is usually due to an underlying mechanism which causes the incoming carriers to ignore the barrier completely; these mechanisms include forbidden backscattering due to topological spin-momentum locked bands and majorana zero-mode assisted tunneling, among others. PAR has three unique identifiers in a differential conductance spectrum: a perfectly flat plateau, the plateau is at twice the conductance of the normal state, and the plateau extends out to the superconducting energy gap.

cite klein  
paper

This bias-independent conductance plateau is observed in other devices with straight edges, however when performing tunneling experiments on “rough” edges (i.e. edges that are not straight) the differential conductance does not show a plateau at low-biases (Fig ). This suggests that the PAR in this system is sensitive to the local contact conditions or the contact to the bulk superconductivity is highly-sensitive to the details of the contact. In the latter case, the PAR is not

Make  
Edge vs  
Plateau  
figure

fig ref

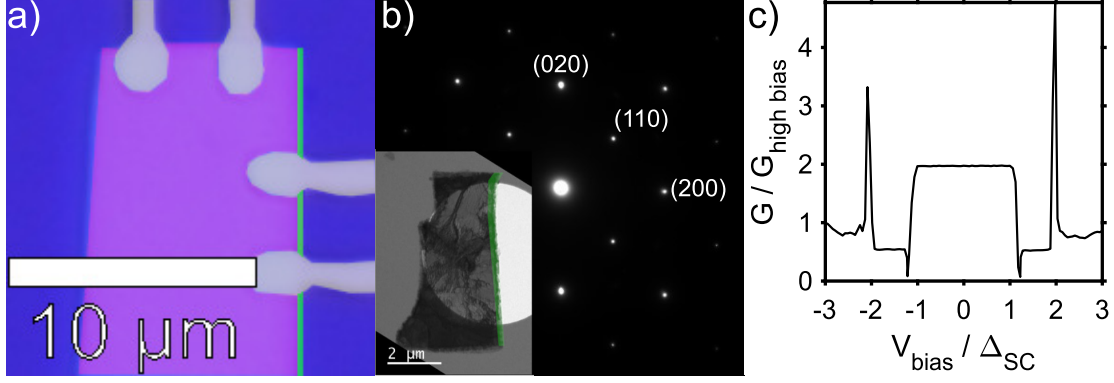


Figure 4.1: a) False color optical image of a representative device with a straight (100) edge. b) TEM diffraction pattern demonstrating the (100) edge. Inset shows the flake measured as well as the diffraction aperture. c) Base temperature differential conductance curve.

affected by the local contact conditions but the signal is drowned out among a much larger supercurrent when better contact is made to the superconducting bulk.

### 4.3 Magnetic Field Dependence

Topological materials are generally highly-sensitive to an external magnetic field, depending on the direction that the field is applied. Indeed, the Dirac surfaces states that are a key signature of a topological bulk are protected via time-reversal symmetry. It follows that if time-reversal symmetry is lifted via a magnetic field, any Dirac nodes that are aligned (the plane perpendicular to the spin-momentum locking determines the “direction” of the cone) along the magnetic field will lose their topological protection. In contrast, if the Dirac node is perpendicular to the magnetic field, the node will simply shift up or down in energy but the node will keep its topological protection. In this manner, if the PAR is caused by forbidden backscattering due to topological bands we expect highly anisotropic responses to different directions of applied magnetic field. While this seems to be the case in FTS (shown in Fig 4.3) we must be careful to differentiate

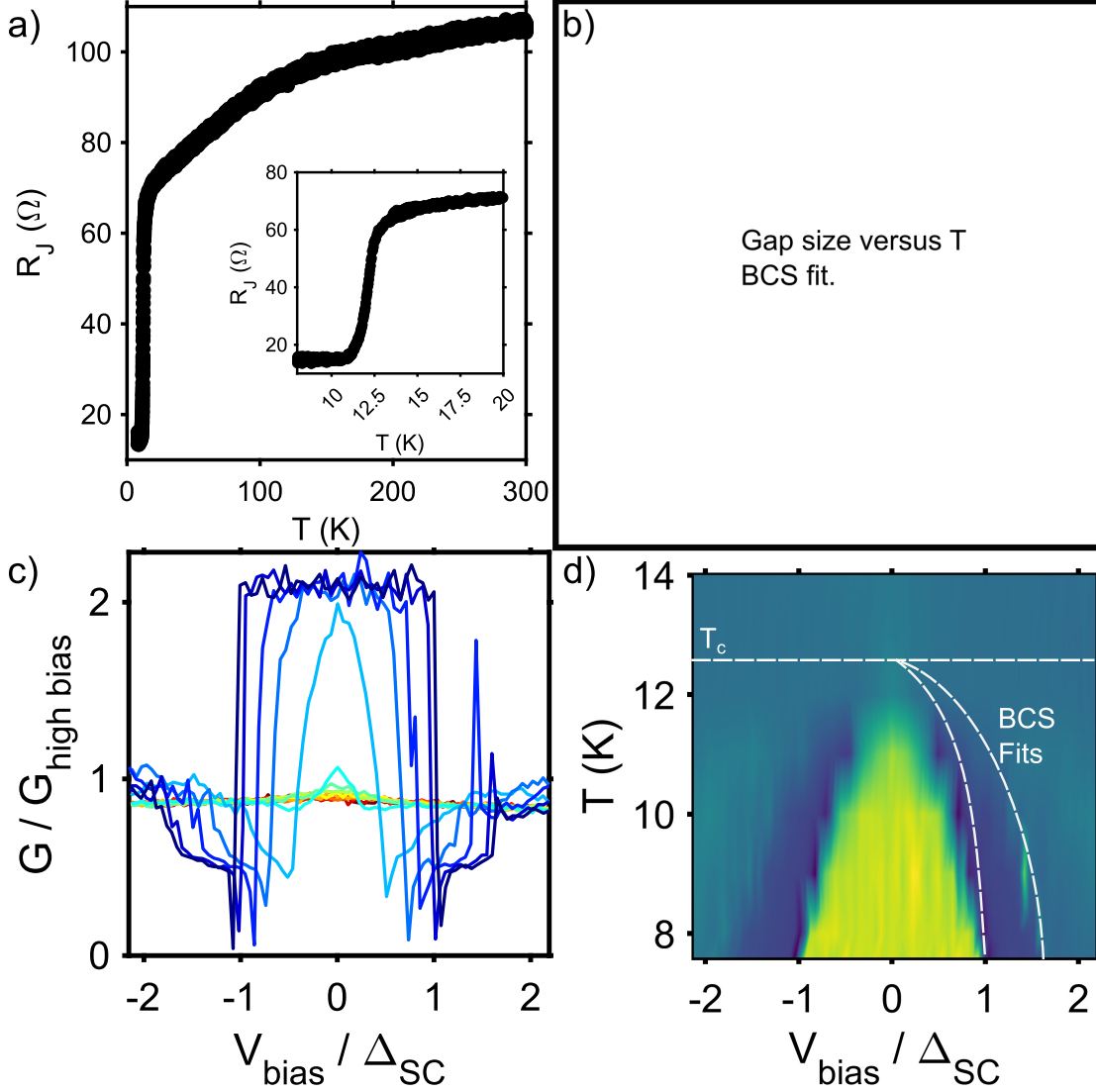


Figure 4.2: Caption

the response of the PAR from that of the bulk superconductor. Even though the upper critical field of FTS is around  $35T$  the bulk superconducting response of FTS flakes is quite anisotropic, even below  $9T$  [zalic2019]. When applying a magnetic field parallel with the hinge being measured (the  $a$ -axis of the material), the PAR remains completely unaffected up to  $5T$ . However, when the field is rotated to the  $c$ -axis of the crystal the PAR seems to collapse quite rapidly which would give credence to a topological origin as discussed earlier.

cite field  
work

## 4.4 Conclusion

In this work we expanded upon the methods used in Chapter . When contacting straight, crystallographic edges we observe Perfect Andreev Reflection while contacts on “rough” edges show normal Andreev Reflection spectra.

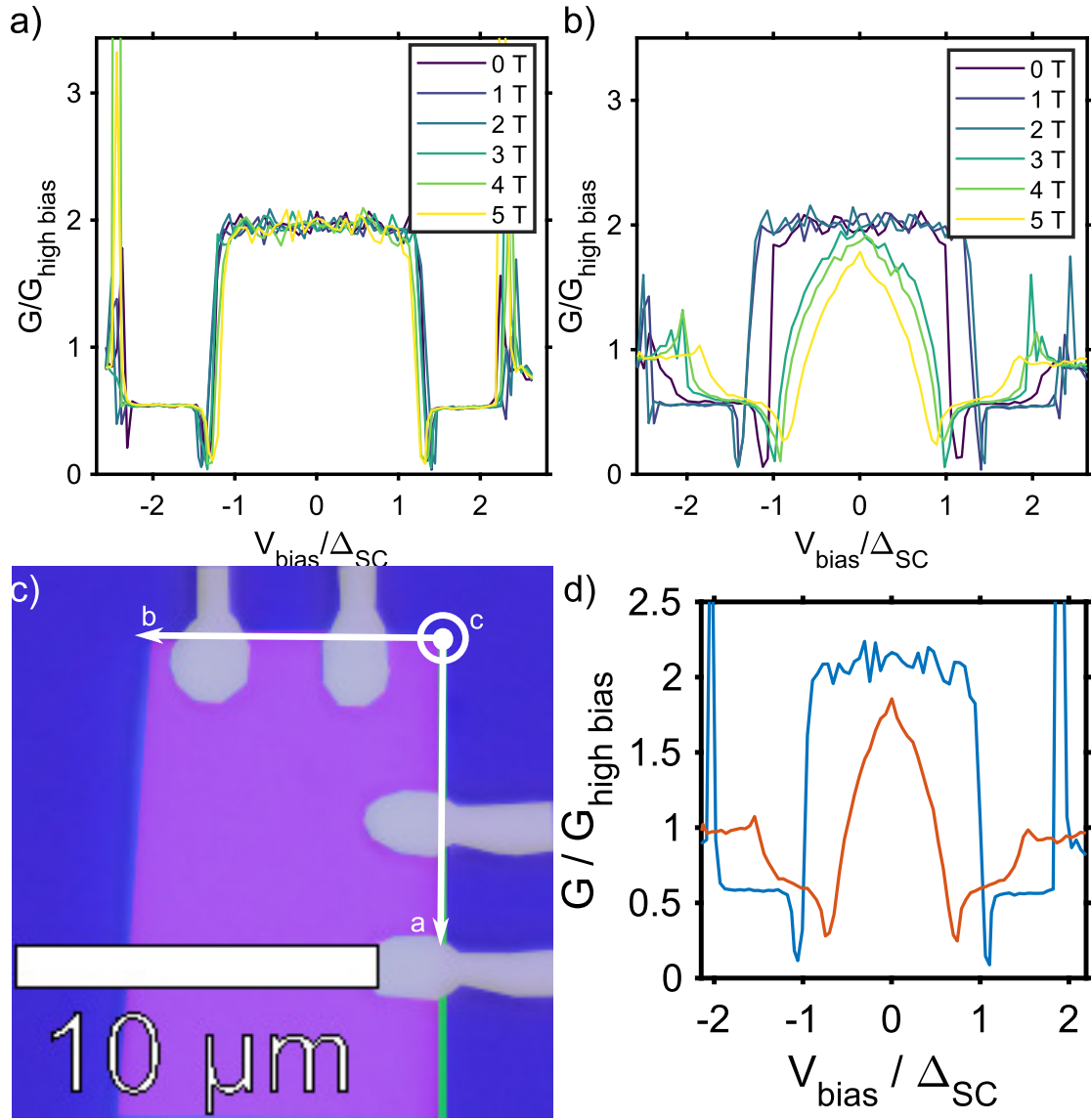


Figure 4.3: Caption

## CHAPTER V

### Conclusion

#### 5.1 Summary

In this dissertation we have presented numerous works investigating the topological nature of iron-based superconductor  $\text{FeTe}_{0.45}\text{Se}_{0.55}$ . To probe the topological nature of FTS we required a fabrication process that consistently left the surfaces and edges of the crystals in pristine condition. Thus in Chapter II we discussed the concept, development, and optimization of the “Cleanroom-in-a-Glovebox”. This glovebox takes the workflow from a standard cleanroom photolithography process and condenses it into an inert argon environment. The merits of such works were demonstrated by comparing the Raman signals of various air-sensitive materials before and after exposure to air. Furthermore, these materials were subsequently fabricated into electronic devices using the photolithography workflow and shown to have similar quality Raman signals, demonstrating the power of the glovebox fabrication process. The linear layout of the fabrication workflow was optimized to maximize the number of available machines as well as minimize the time between fabrication steps. In addition to powerful fabrication and characterization abilities, the glovebox is also a perfect tool for training the next generation quantum workforce. The simple interfaces of the fabrication facil-

Write summary of FTS and glovebox. Give ideas for new experiments.

ities provide a low-stress situation for scientists to learn nanofabrication without fear of breaking the equipment. The conveyor-belt layout of the glovebox takes the mental load off of the student-scientists so they can focus on the creative and fun aspects of creating mesoscopic devices.

In Chapter III we presented strong evidence for a normal mode that exists purely on the hinge or the side of the FTS crystal in the superconducting state. Recent theoretical work has suggested that such a mode could be the result of the combination of an exotic  $s^\pm$  order parameter and a topological surface state. In short, the anisotropy of the superconducting phase gaps out adjacent faces of the Topological Insulator (TI) causing a normal mode at zero energy to appear at the hinge between the top and side surfaces.

Finally, in Chapter IV we extend the scope of our electronic spectroscopy probe of FTS to undercover exciting underlying physics.

## **5.2 Future Work**

Beyond finishing the work put forth in Chapter IV, there is a clear and exciting road forward for FTS and other topological superconductors. Here I lay out some experiments I believe would provide interesting insight into the fundamental physics of FTS.

### **5.2.1 Fe-based topological superconductivity**

In Chapter IV we touched on the concept of symmetries protecting topologies. This work provided evidence that there is an important symmetry on the  $[100]$  face of the FTS crystal but it would be useful to elucidate whether this is actually due to the  $c_4$  symmetry. Here I suggest performing a series of three-point measurements shown in Chapters III and IV on a variety of crystal facets: specifically on the  $[100]$ ,  $[110]$ , and  $[010]$  facets as these would provide the strongest implication of the



c4 symmetry. To accomplish this, one would naturally also need a new fabrication process to cut the exfoliated crystal into pristine edges. Here we suggest either RIE (in the fashion of graphene heterostructure devices), FIB (such as the beautiful devices shown in the work of G. B. Osterhoudt[**Osterhoudt2019**]), or shadow-mask techniques while growing MBE thin-films.

## APPENDICES

## APPENDIX A

### Pseudocode for Andreev Reflection fitting

As mentioned in the main text, Andreev Reflection is the process by which an electron is reflected as a hole at the interface between a normal-metal / superconductor interface. By modeling and fitting our data to this model we are able to extract useful quantities such as the superconducting gap size (at a specific temperature), the transparency of the interface, and the thermal broadening of our spectra from our junction size. Thus, here I layout a condensed version of the BTK calculation for differential conductance across a normal-metal / superconducting interface then I go through pseudo-code on how to fit this calculation to our data.

#### A.1 BTK Theory

In 1964, Alexander F. Andreev published a paper describing a process by which an electron incident upon a superconductor forms a cooper pair in the superconductor and retro-reflects a hole[**Andreev1964**]. This phenomena was originally used to describe the thermal conductivity properties observed in superconductors in the intermediate state where there are many normal sections in direct contact with superconducting sections. It wasn't until 1982 that Blonder, Tinkham,

and Klapwijk gave a complete discussion of the phenomena including the effect of the barrier magnitude, a model for the excess current, and predictions for the differential conductance of such a junctions[BTK].

### A.1.1 The BdG Formalism

The key innovation in the BTK model is the use of the BdG equations to match the wavefunctions of the quasi-particles excitations at the interface[BTK]. Here I will closely follow the explanation of the BdG equations shown in Chapter 14 of "Topological Insulators and Topological Superconductivity" by Bernevig and Hughes[bernevig'hughes'2013]. First we start with the Hamiltonian for a single-particle in a simple metal.

$$H = \left( \frac{p^2}{2m} - \mu \right) I_{2 \times 2} \quad (\text{A.1})$$

Where  $\mu$  is the chemical potential and  $I_{2 \times 2}$  is the identity matrix in the spin variables. The second-quantized Hamiltonian is given by:

$$H = \sum_{\mathbf{p}, \sigma} c_{\mathbf{p}\sigma}^\dagger \left( \frac{p^2}{2m} - \mu \right) c_{\mathbf{p}, \sigma} \quad (\text{A.2})$$

Where  $c^\dagger$  and  $c$  are the quasi-particles creation and annihilation operators respectively. Using the anti-commutativity relation of fermions,  $\{c_{\mathbf{p}\sigma}^\dagger, c_{\mathbf{p}'\sigma'}\} = \delta_{\sigma\sigma'}\delta_{\mathbf{p}\mathbf{p}'}$ , we can rewrite the Hamiltonian above as,

$$H = \frac{1}{2} \sum_{\mathbf{p}\sigma} \left[ c_{\mathbf{p}\sigma}^\dagger \epsilon(p) c_{\mathbf{p}\sigma} - c_{-\mathbf{p}\sigma} \epsilon(-p) c_{-\mathbf{p}\sigma}^\dagger \right] + \frac{1}{2} \sum_p \epsilon(p) \quad (\text{A.3})$$

Where  $\epsilon(p) \equiv \left( \frac{p^2}{2m} - \mu \right)$  and we have relabeled the sum index  $\mathbf{p}$  in the second term to  $-\mathbf{p}$ . Here we introduce a new spinor to explicitly label the energy eigenvalues for both spins of both  $\epsilon_p$  and  $\epsilon_{-p}$ . E.g., we define  $\Psi_{\mathbf{p}} \equiv \left( c_{\mathbf{p}\uparrow} c_{\mathbf{p}\downarrow} c_{-\mathbf{p}\uparrow}^\dagger c_{-\mathbf{p}\downarrow}^\dagger \right)$ , then we

can rewrite the above Hamiltonian as,

$$H = \sum_{\mathbf{p}} \Psi_{\mathbf{p}}^{\dagger} H_{BdG}(\mathbf{p}) \Psi_{\mathbf{p}} + \text{constant} \quad (\text{A.4})$$

$$H_{BdG}(\mathbf{p}) = \frac{1}{2} \begin{pmatrix} \epsilon(p) & 0 & 0 & 0 \\ 0 & \epsilon(p) & 0 & 0 \\ 0 & 0 & -\epsilon(-p) & 0 \\ 0 & 0 & 0 & -\epsilon(-p) \end{pmatrix} \quad (\text{A.5})$$

The point of this formalism becomes immediately apparent when we introduce a superconducting pairing potential.

$$H_{\Delta} = \Delta c_{\mathbf{p}\uparrow}^{\dagger} c_{-\mathbf{p}\downarrow}^{\dagger} + \Delta^* c_{-\mathbf{p}\downarrow} c_{\mathbf{p}\uparrow} \quad (\text{A.6})$$

$$= \frac{1}{2} \left[ \Delta \left( c_{\mathbf{p}\uparrow}^{\dagger} c_{-\mathbf{p}\downarrow}^{\dagger} - c_{-\mathbf{p}\downarrow}^{\dagger} c_{\mathbf{p}\uparrow}^{\dagger} \right) + \Delta^* \left( c_{-\mathbf{p}\downarrow} c_{\mathbf{p}\uparrow} - c_{\mathbf{p}\uparrow} c_{-\mathbf{p}\downarrow} \right) \right] \quad (\text{A.7})$$

$$\therefore H + H_{\Delta} = \sum_{\mathbf{p}} \Psi_{\mathbf{p}}^{\dagger} H_{BdG}(\mathbf{p}, \Delta) \Psi_{\mathbf{p}} \quad (\text{A.8})$$

$$H_{BdG}(\mathbf{p}, \Delta) = \frac{1}{2} \begin{pmatrix} \epsilon(p) & 0 & 0 & \Delta \\ 0 & \epsilon(p) & -\Delta & 0 \\ 0 & -\Delta^* & -\epsilon(-p) & 0 \\ \Delta^* & 0 & 0 & -\epsilon(-p) \end{pmatrix} \quad (\text{A.9})$$

Using this formalism, we can see that the pairing potential simply couples the upper and lower blocks of the  $H_{BdG}$  for the simple metal Hamiltonian. From here we can diagonalize  $H_{BdG}$  to obtain the energy eigenvalues.

$$E_{\pm} = \pm \sqrt{\epsilon(\mathbf{p})^2 + |\Delta|^2} \quad (\text{A.10})$$

The quasi-particles dispersion relations for the normal metal ( $|\Delta| = 0$ ) and the superconductor ( $|\Delta| = 0.1m$ ) are plotted in Fig A.1 which also conveniently serves

as a perfect starting point for the discussion of the BTK calculation.

### A.1.2 The BTK calculation

First, we consider a normal metal in contact with a superconductor. The dispersion relations for the two are as calculated in the previous section and the barrier in the interface is modeled by a Dirac-delta function with magnitude  $Z$ . BTK considers a plane-wave electron incident from the normal metal on the left side of the junction thus when the electron encounters the barrier there are four possibilities (shown in Fig A.1):

- A) The electron is Andreev reflected as a left-moving hole and a right-moving Cooper-Pair transmits into the superconducting fluid.
- B) The electron is specularly reflected as a left-moving electron.
- C) The electron is transmitted as a right-moving electron-like quasiparticle.
- D) The electron is transmitted as a right-moving hole-like quasiparticle.

To solve for the probabilities of each process occurring we first define the momenta in the normal metal and superconductor respectively as,

$$k^{\pm} = \sqrt{\frac{2m_N}{\hbar^2}} \sqrt{E_{FN} \pm E} \quad (\text{A.11})$$

$$q^{\pm} = \sqrt{\frac{2m_{SC}}{\hbar^2}} \sqrt{E_{FSC} \pm \sqrt{E^2 - \Delta^2}} \quad (\text{A.12})$$

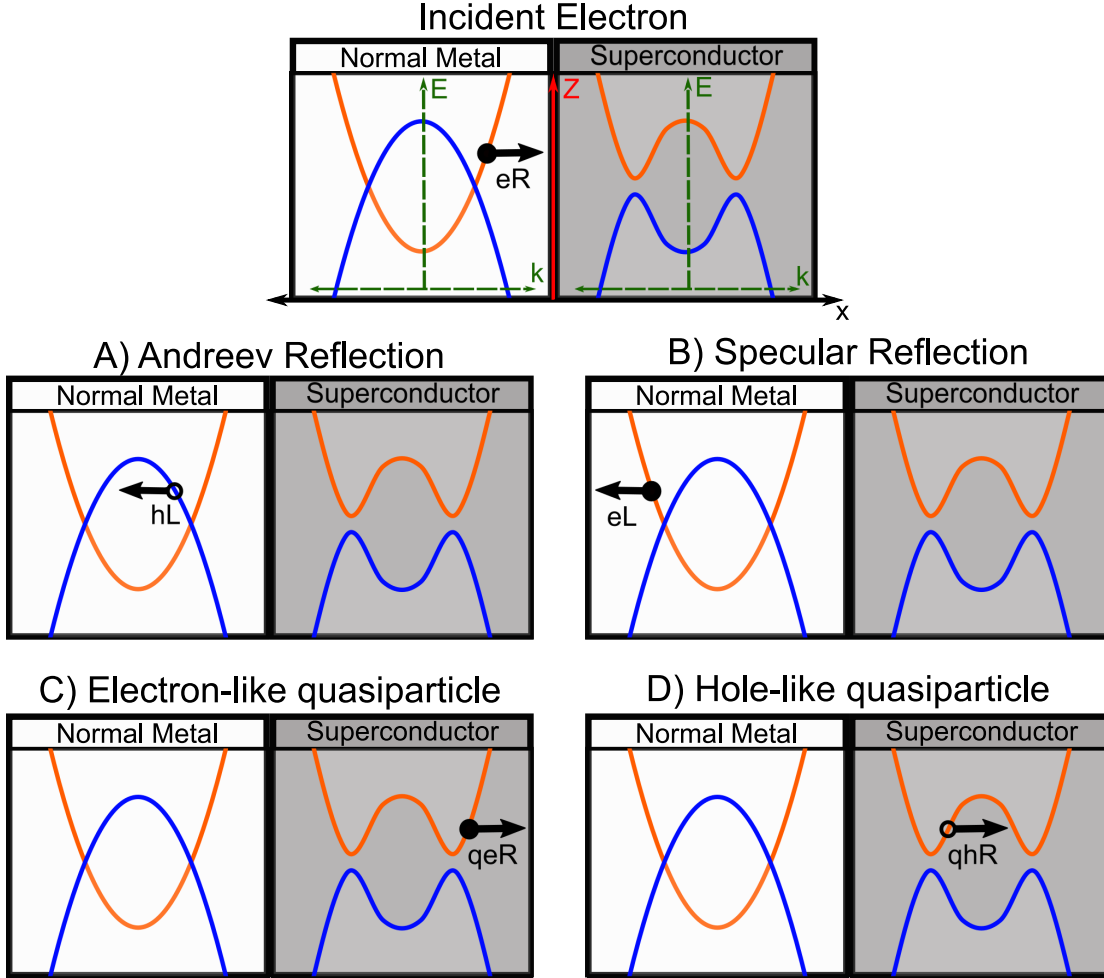


Figure A.1: Dispersion relations for a normal metal and superconductor in physical contact with one another. The red axis denotes the real-space position of the two materials with a potential barrier at their interface. The subset green, dashed axes denote the dispersion relations within the respective materials. A right-moving incident electron (top) can take one of four paths once it hits the NM/SC barrier: A) Andreev reflect as a left-moving hole, B) Normally reflect as a left-moving electron, C) Transmit as a right-moving electron-like quasi-particles, or D) Transmit as a right-moving hole-like quasi-particles.

Then we simply match the boundary conditions, i.e., the wavefunctions and their derivatives are the same at the boundary. Starting with the wavefunctions,

$$\begin{pmatrix} 1 \\ 0 \end{pmatrix} e^{ik^+x_0} + C \begin{pmatrix} 1 \\ 0 \end{pmatrix} e^{-ik^+x_0} + D \begin{pmatrix} 0 \\ 1 \end{pmatrix} e^{ik^-x_0} = A \begin{pmatrix} u_0 \\ v_0 \end{pmatrix} e^{iq^+x_0} + B \begin{pmatrix} u_0 \\ v_0 \end{pmatrix} e^{-iq^-x_0} \quad (\text{A.13})$$

then the derivatives.

$$\frac{\hbar^2}{2m_N} \left\{ ik^+ \begin{pmatrix} 1 \\ 0 \end{pmatrix} e^{ik^+x_0} - ik^+ C \begin{pmatrix} 1 \\ 0 \end{pmatrix} e^{-ik^+x_0} + ik^- D \begin{pmatrix} 1 \\ 0 \end{pmatrix} e^{ik^-x_0} \right\} \quad (\text{A.14})$$

$$= \frac{\hbar^2}{2m_{SC}} \left\{ iq^+ A \begin{pmatrix} u_0 \\ v_0 \end{pmatrix} e^{iq^+x_0} - iq^- B \begin{pmatrix} u_0 \\ v_0 \end{pmatrix} e^{-iq^-x_0} \right\} \quad (\text{A.15})$$

$$+ H * \left\{ A \begin{pmatrix} u_0 \\ v_0 \end{pmatrix} e^{iq^+x_0} + B \begin{pmatrix} u_0 \\ v_0 \end{pmatrix} e^{-iq^-x_0} \right\} \quad (\text{A.16})$$

where  $x_0$  is the position of the barrier (it is typically set to zero) and  $u_0, v_0$  are the electron-weight and hole-weight of the quasiparticles, respectively. Thus the transmission coefficients are given by:

$$\begin{aligned} a &= (|A|^2 * (u_0^2 - v_0^2)) \frac{q_{SC}^+}{k_N^+} & b &= |B|^2 * (u_0^2 - v_0^2) \frac{q_{SC}}{k_N^+} \\ c &= |C|^2 & d &= |D|^2 * \frac{k_N^-}{k_N^+} \end{aligned} \quad (\text{A.17})$$

Before plugging in the momentum values there are some quick simplification we can make here to improve readability. Using,  $v_F^{SC} = \hbar k_{FSC}/m_{SC}$  and  $v_{FN} = \hbar k_{FN}/m_N$ , we define  $Z_0 \equiv H/\hbar\sqrt{v_{FN} * v_{SC}}$ . Now we can define the  $Z$  parameter



that will characterize the potential barrier as:

$$Z^2 \equiv Z_0^2 + \frac{(1 - r_v^2)}{4r_v} \quad (\text{A.18})$$

$$r_v \equiv \frac{v_{FN}}{v_{FSC}} = \sqrt{\frac{E_{FN}m_{SC}}{E_{FSC}m_N}} \quad (\text{A.19})$$

so that we can set  $E_{FN} = E_{FSC}$  and  $m_N = m_{SC}$ . Next, we set  $\gamma = u_0^2 + (u_0^2 - v_0^2)Z^2$ . Finally, we note that the solution is vastly different in the two scenarios where  $E < \Delta$  and  $E > \Delta$  thus it behooves us to write them as a piece-wise function.

$$\begin{aligned} a(E) &= \begin{cases} 0 & E < \Delta \\ \frac{(u_0^2 - v_0^2)u_0^2(1+Z^2)}{\gamma^2} & E \geq \Delta \end{cases} & b(E) &= \begin{cases} 0 & E < \Delta \\ \frac{(u_0^2 - v_0^2)v_0^2Z^2}{\gamma^2} & E \geq \Delta \end{cases} \\ c(E) &= \begin{cases} \frac{4Z^2(1+Z^2)(\Delta^2 - E^2)}{E^2 + (\Delta^2 - E^2)(1+2Z^2)^2} & E < \Delta \\ \frac{(u_0^2 - v_0^2)Z^2(1+Z^2)}{\gamma^2} & E \geq \Delta \end{cases} & d(E) &= \begin{cases} \frac{\Delta^2}{E^2 + (\Delta^2 - E^2)(1+2Z^2)^2} & E < \Delta \\ \frac{u_0^2v_0^2}{\gamma^2} & E \geq \Delta \end{cases} \end{aligned} \quad (\text{A.20})$$

Thus we can simply read-off the differential conductance across the junction as:

$$\sigma = 2 * d(E) + a(E) + b(E)$$

The plots for various potential barrier strengths ( $Z$ ) are shown in Fig A.2 along with some other corrections in the next section.

## A.2 Pseudo-Code for fitting spectra

Tunneling in a normal metal/superconductor interface can produce wildly different spectra depending on the various parameters such as temperature, barrier height, disorder, and more. This pseudo-code was written to characterize such superconducting tunneling spectra via the 1D BTK model and extract information

such as the superconducting gap. The results of running each individual algorithm are shown in Fig A.2 to show how each parameters affects a tunneling spectrum, however in most cases one will need to use two or more of these algorithms in concert to obtain a good fit for a spectrum. For a full extension of the model to 2D, 3D, and unconventional superconductivity please read the in-depth topical reviews by D. Daghero & R. S. Gonnelli[Daghero2010] and Kashiwaya & Tanaka[Kashiwaya2000].

First we write a function (Algorithm 1) that calculates the BTK conductance spectra at zero temperature. The inputs to this functions are: the measured voltage vector in millivolts (meV), the barrier height (Z), the superconducting energy gap ( $\Delta_{SC}$ ), and the thermal broadening parameter ( $\Gamma$ ). This code is useful

---

**Algorithm 1** Single Gap BTK conductance

---

```

1: function BTK1G(meV, Z,  $\Delta_{SC}$ ,  $\Gamma$ )                                ▷ Returns conductance vector.
2:    $N_q = \left| \frac{meV+i\Gamma}{\sqrt{(meV+i\Gamma)^2 - \Delta_{SC}^2}} \right|$                 ▷ quasi-particles Density of States (DoS)
3:    $N_p = \frac{\Delta_{SC}}{\sqrt{(meV+i\Gamma)^2 - \Delta_{SC}^2}}$                         ▷ Pair DoS
4:    $\tau_n = \frac{1}{1+Z^2}$                                                 ▷ Define the transparency
5:    $\gamma = \frac{N_q-1}{N_p}$                                                 ▷ Define  $\gamma$  function. Not  $\Gamma$ !
6:    $G = \frac{1+\tau_n|\gamma|^2+(\tau_n-1)|\gamma^2|^2}{|1+(\tau_n-1)\gamma^2|^2}$                 ▷ G will be a vector.
7:   return  $G, \tau_n$                                                 ▷ We return  $\tau_n$  in preparation for the next function.
8: end function

```

---

for understanding what the conductance looks like at various Z-values, Gap-sizes. The broadening term can be used (or fit) to simulate a finite temperature since (as the name suggests) it is basically a term that broadens the spectral peaks out.

If we want to incorporate the temperature in a more rigorous way we can take the outputs of the previous function then integrate the convolution of their product with the Fermi function (Algorithm 2). I've used an anonymous function since these codes were originally written in MatLab however the same task can be accomplished in Python with a lambda function instead. Alternatively, one could also

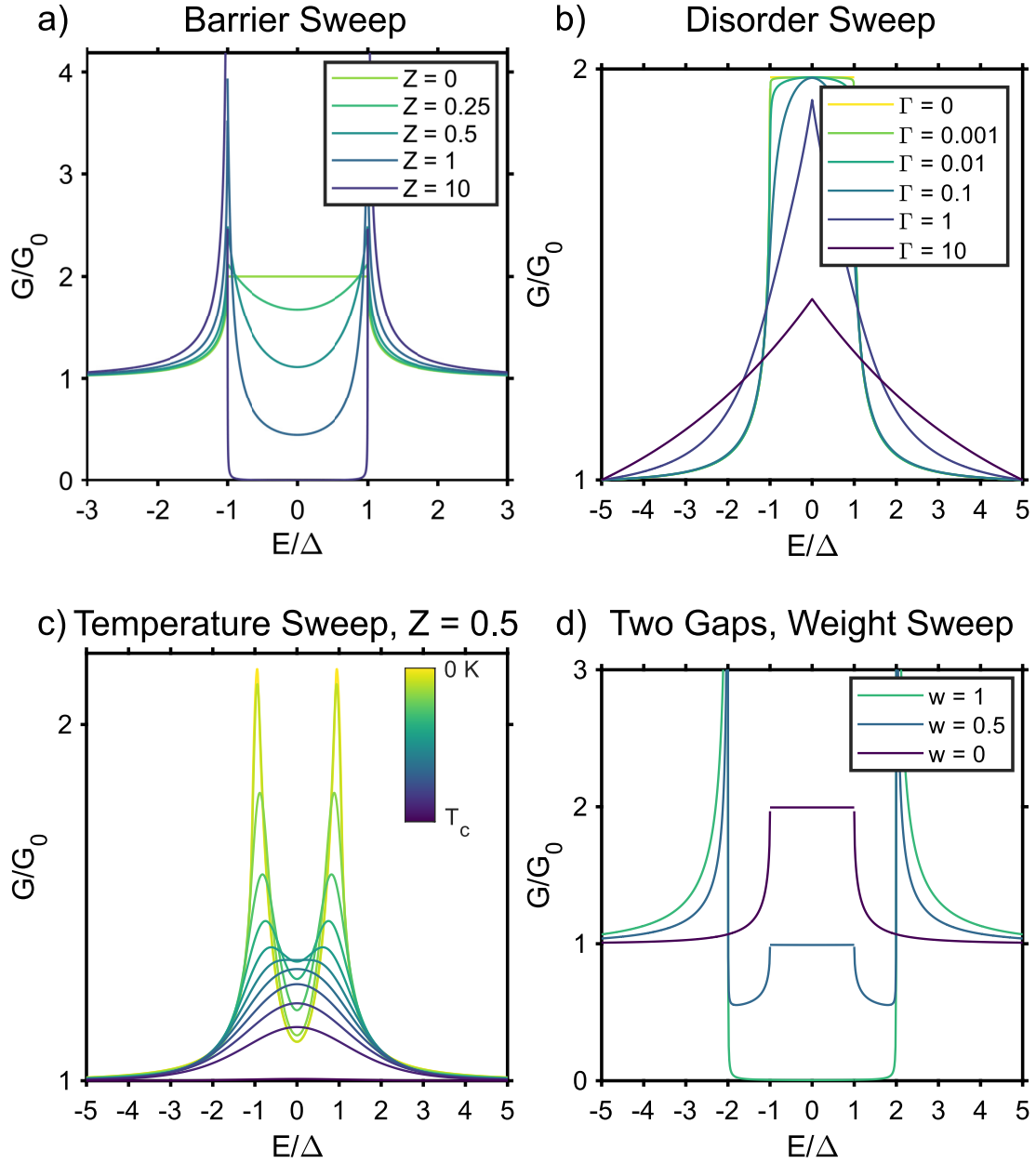


Figure A.2: Various demonstrations of the differential conductance calculated using the algorithms described in A.2. a) Single gap, zero Kelvin sweep of the potential barrier strength  $Z$ . b) Single gap, zero Kelvin, zero barrier sweep of the thermal broadening parameter  $\Gamma$ . c) Single gap, half-strength barrier, temperature sweep. d) Two superconducting gaps where the second gap is twice as large as the first demonstrating the  $w$  parameter in action.

---

**Algorithm 2** BTK at finite temperature

---

```
1:  $G, \tau_n = BTK1g(meV, Z, \Delta_{SC}, \Gamma)$ 
2: for V in meV do
3:    $f_C = G\tau_n \left( \frac{1}{e^{(e-V)/k_bT}} - \frac{1}{e^{E/k_bT+1}} \right)$   $\triangleright$  Convolution. Outputs a function.
4:    $I_{ns}(V) = \int_{-\infty}^{\infty} f_C dE$   $\triangleright$  Integrate function over all energies.
5: end for
6:  $\frac{dI}{dV} = |\nabla(I_{NS})|$ 
```

---

skip the for-loop by implementing the numpy function `numpy.convolve(vector1,vector2)`.

Algorithm 3 is a simple extension that allows us to model the conductance with two superconducting gaps.

---

**Algorithm 3** Two Gap BTK Fit

---

BTK\_2Gap

```
 $G_1, \tau_1 = BTK\_at\_finite\_temperature(meV, Z_1, \Delta_{SC,1}, \Gamma_1)$ 
 $G_2, \tau_2 = BTK\_at\_finite\_temperature(meV, Z_2, \Delta_{SC,2}, \Gamma_2)$ 
 $G = w * G_1 + (w - 1) * G_2$   $\triangleright w$  ranges between 0 and 1.
```

---

Algorithm 4 is another simple function to either fit the temperature-dependence of the gaps to what's predicted via BCS theory or use this function to generate a series of gap sizes for our BTK versus temperature function later. I've presented this as a function so that it's easier to fit with, but this can be defined as an anonymous function (MatLab) or lambda function (Python) to reduce file complexity. Finally Algorithm 5 denotes the whole script for modelling and plotting

---

**Algorithm 4** BCS Gap

---

```
1: function BCSGAP( $T, \Delta_0, T_c, \alpha$ )  $\triangleright$  SC gap at temperature T.
2:    $\Delta(T) = \left| 1.74k_bT_c \left( 1 - \left( \frac{T}{T_c} \right)^\alpha \right) \right|$ 
3:   return  $\Delta(T)$ 
4: end function
```

---

a range of temperatures to both single gap and two-gap BTK models using the above functions. Fitting the function varies by platform a bit but the pseudo-code is to define the "BTK and finite temperature" file as the model as use the built-in fit functions.

---

**Algorithm 5** BTK Temperature Fit

---

BTKTempFit

```
1: Temps, dataCell = loadData(folder) ▷ “load_data” is a script written by G.
   Osterhoudt.
2: fig = figure(1) ▷ Can use plt.subplot in Python
3: G0 = zeros(length(Temps)) ▷ Will populate with normalization.
4: j = 0 ▷ Iteration variable
5: for T in Temps do
6:    $\Delta_{SC} = BCSGap(T, \Delta_0, T_c, \alpha)$ 
7:   G = BTK_at_finite_temperature(meV, Z, ΔSC, Γ)
8:   Smooth
9:   G0(j) = G(end)
10:  j + = 1
11:  plot(meV, G/G0)
12: end for
```

---

## APPENDIX B

### Model of the differential conductance circuit

As discussed in Chapter III, we are interested in measuring the differential conductance of samples versus a DC bias voltage. This is because the differential conductance of a normal sample is directly proportional to the DoS of a material. To see this, let's start off by considering the contribution of a single carrier tunneling from our contact to the sample, we also must consider carriers tunneling from the sample to the contact:

$$i_{sample \rightarrow contact} = -2e \frac{2\pi}{\hbar} |M|^2 (\rho_s(\varepsilon) \cdot f(\varepsilon)) \cdot (\rho_c(\varepsilon - eV) \cdot [1 - f(\varepsilon - eV)]) \quad (\text{B.1})$$

$$i_{contact \rightarrow sample} = -2e \frac{2\pi}{\hbar} |M|^2 (\rho_c(\varepsilon - eV) \cdot f(\varepsilon - eV)) \cdot (\rho_s(\varepsilon) \cdot [1 - f(\varepsilon)]) \quad (\text{B.2})$$

Where  $|M|^2$  is the tunneling matrix element which describes the specifics of the junction (for an excellent breakdown of how this matrix function corresponds to different junction types see Berthod (2011)[**Berthod2011**]),  $\rho_{s,c}$  is the DoS of the sample and contact respectively, and  $f(\varepsilon)$  is the Fermi function. To get the total current across this junction we sum the contribution from both directions and

integrate over all energies.

$$I = -\frac{4\pi e}{\hbar} \int_{-\infty}^{\infty} |M|^2 \rho_s(\varepsilon) \rho_c(\varepsilon - eV) [f(\varepsilon) \cdot [1 - f(\varepsilon - eV)] - f(\varepsilon - eV) \cdot [1 - f(\varepsilon)]] d\varepsilon \quad (\text{B.3})$$

Here we take the derivative with respect to  $\varepsilon$  to get:

$$\frac{dI}{d\varepsilon} = -\frac{4\pi e}{\hbar} |M|^2 \rho_s(\varepsilon) \rho_c(\varepsilon - eV) [f(\varepsilon) \cdot [1 - f(\varepsilon - eV)] - f(\varepsilon - eV) \cdot [1 - f(\varepsilon)]] \quad (\text{B.4})$$

Thus at a given bias voltage (eV) and temperature the differential conductance is proportional to the product of the densities of states of the sample and contact. Therefore if the contact has a constant DoS in energy, the differential conductance is directly proportional to the DoS of the sample.

When probing a sample in the superconducting state, the differential conductance can be used to probe the superconducting characteristics of the system. As an example, the BTK theory discussed in Appendix A demonstrates how to use the differential conductance versus bias voltage curve to determine the magnitude of the superconducting energy gap.

## B.1 Measuring differential conductance

One method of measuring the differential conductance is to measure the current-voltage characteristics and then take a numerical derivative. This can be time-consuming to get enough data to ensure a low-noise  $\frac{dI}{dV}$  curve and can lead to resolution limitations. An alternate method is to add a small AC voltage on top of the DC voltage then measure the resulting AC current. In this case, we can

express the current response as a Taylor series:

$$I(V + v \cos(\omega t)) = I(V) + \frac{dI}{dV} v \cos(\omega t) + \frac{1}{2} \frac{d^2 I}{dV^2} v^2 \cos^2(\omega t) + \dots \quad (\text{B.5})$$

Thus the signal measured at frequency  $\omega$  will be proportional to the first derivative of the current-voltage characteristics. We can therefore use a Lock-In Amplifier (LIA) to directly measure the differential conductance without any numerical processing. Then we can probe the DoS for a range of the band structure by sweeping the bias voltage and measuring the  $\frac{dI}{dV}$  at every point.

## B.2 Circuit construction

Now let's see how this model is executed in the lab by examining the AC + DC adder circuit in more detail. The circuit as of May 2021 is shown in B.1. As we are interested in measuring the bias voltage across the junction (rather than the bias current) we start by sending in a DC voltage (point A) with a BK Precision 1785b. Given that this power supply only has 10 mV resolution and that the spectroscopic features we are searching for are of order 1 mV, we need to use a voltage divider (point B). This voltage divider introduces some problems that will be discussed in the next section. The AC voltage is then added to the DC voltage via a one-to-one transformer (point C) which has the added benefits of isolating the AC signal from the rest of the circuit. The AC signal can be sent through an attenuating circuit first if the current is too large. To find the current going through the sample we either insert a resistor in series with the sample or use a current pre-amplifier (pre-amp) but in both cases, the AC and DC voltages over the resistor (or output from the pre-amp) are measured in parallel (point E). The current going through the sample is then simply the measured voltage divided by the resistor (or 1/sensitivity if using the pre-amp). We also measure the AC



and DC voltages at the sample so that we do not need to assume the voltages we output are actually what is placed across the sample (point D).

### B.2.1 Circuit troubles and solutions

The SR-570 Low Noise Current Preamplifier was found to send out a large voltage spike ( $\sim 1\text{V}$ !) across the circuit when switching sensitivities, which often damaged or destroyed the device. For this reason we switched to using the resistor method. For higher resistance devices in which a pre-amp is needed to measure a much smaller current it is recommended that the user ground the device, disconnect the pre-amp, make the gain and sensitivity adjustments, then reconnect and unground the device. This is a slow process but it will ensure the pre-amp voltage spike does not damage the device under test.

The governing physics behind the voltage divider is shown in the equation,

$$V_{out} = V_{in} * \frac{R_2}{R_1 + R_2} \quad (\text{B.6})$$

however this model assumes that the output voltage is over an open circuit meaning that the resistance of the sample is large compared to  $R_2$ . When samples have a small resistance, the output voltage can change drastically from the expected value. This is especially concerning when the resistance of a sample changes drastically over a single measurement as can be the case when measuring superconducting tunneling. One solution is to use commercial voltage regulators to ensure a steady voltage is maintained even at high currents. However, most of these commercial voltage regulators have a minimum voltage output around  $1.2\text{ V}$  which is three orders of magnitude larger than our  $1\text{ mV}$  resolution requirement. Another solution is to switch to current-biased measurements when dealing with low-resistance samples however converting back to bias voltage can be quite tricky

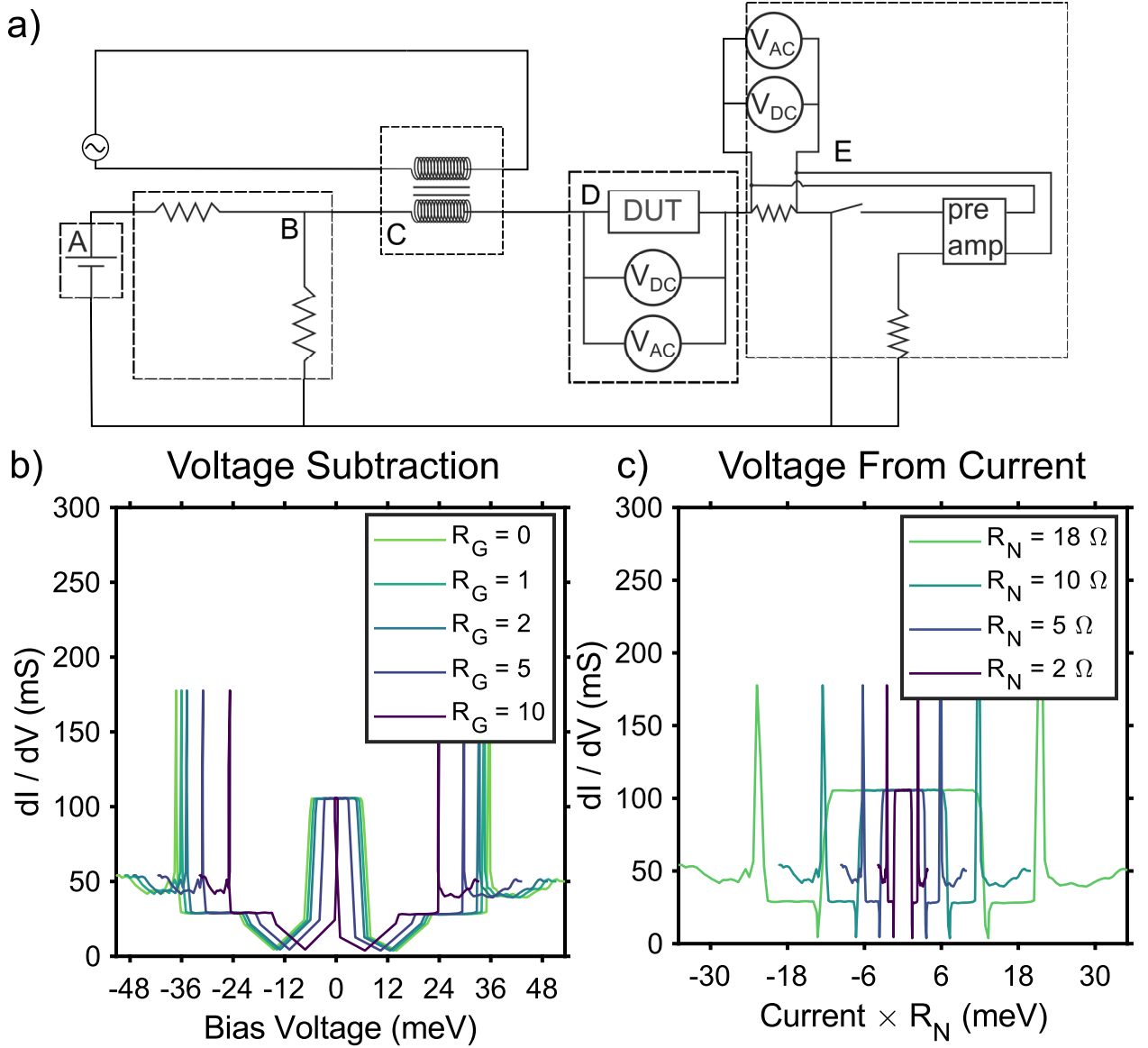


Figure B.1: a) Circuit diagram to add AC and DC voltages then measure differential conductance as a function of applied DC bias. b) Voltage correction of data in Chapter IV via subtraction of extra measured voltage due to the system resistances along the way. c) Voltage correction of the same data by measuring the resulting current and multiplying it by the normal resistance.

as will be discussed in the next section. Lastly would be to simply use a commercial high-resolution DC voltage source such as the DC205 DC Voltage Source from SRS in order to eliminate the voltage divider completely. These sources can be quite expensive but offer resolutions down to the  $\mu\text{V}$  level.

### B.3 Three-point measurements

Lastly, I would like to discuss some peculiarities with the three-point measurements used in Chapters III & IV. In particular, since we use the measured voltage across the junction as our bias voltage (independent axis) we need to carefully consider what voltage is actually being applied across the relevant part of the junction. To illustrate, the reason a four-probe (Kelvin) measurement is preferred when determining a sample's resistivity is the Kelvin resistance does not include contact resistance[Kuphaldt2015]. However in our measurement the quantity that we are measuring *is* the contact resistance thus we want to be sure we don't split that resistance out of our measurement. This presents an issue as the resistance of the chrome/gold contacts will also stay in the measurement and add additional voltage to our bias voltage reading. There are two ways to correct for this: 1) Use the resistivity of a control chrome/gold device to subtract out the resistance (and voltage) or 2) convert the measured current back to a voltage by multiplying by the normal state resistance of the junction. The results of both correct are shown below for varying values of gold resistance.

## BIBLIOGRAPHY